

Spin-directed network model for the surface states of weak three-dimensional \mathbb{Z}_2 topological insulators

Hideaki Obuse

Department of Applied Physics, Hokkaido University, Sapporo 060-8628, Japan

Shinsei Ryu

Department of Physics, University of Illinois, 1110 West Green St, Urbana IL 61801, USA

Akira Furusaki

*Condensed Matter Theory Laboratory, RIKEN, Wako, Saitama 351-0198, Japan and
RIKEN Center for Emergent Matter Science (CEMS), Wako, Saitama 351-0198, Japan*

Christopher Mudry

Condensed matter theory group, Paul Scherrer Institute, CH-5232 Villigen PSI, Switzerland

(Dated: October 5, 2013)

A two-dimensional spin-directed \mathbb{Z}_2 network model is constructed that describes the combined effects of dimerization and disorder for the surface states of a weak three-dimensional \mathbb{Z}_2 topological insulator. The network model consists of helical edge states of two-dimensional layers of \mathbb{Z}_2 topological insulators which are coupled by time-reversal symmetric interlayer tunneling. It is argued that, without dimerization of interlayer couplings, the network model has no insulating phase for any disorder strength. However, a sufficiently strong dimerization induces a transition from a metallic phase to an insulating phase. The critical exponent ν for the diverging localization length at metal-insulator transition points is obtained by finite-size scaling analysis of numerical data from simulations of this network model. It is shown that the phase transition belongs to the *two-dimensional symplectic universality class* of Anderson transition.

I. INTRODUCTION

A strong d -dimensional topological band insulator is a band insulator of noninteracting electrons which is characterized by a nontrivial topological index under certain symmetry constraints. Its $(d-1)$ -dimensional boundary always has gapless boundary states which are extended on the boundary but localized in the direction normal to the boundary. They share, because of the nontrivial topological index, a degree of robustness to perturbations that respect the symmetry constraints.

The simplest example of a strong two-dimensional topological band insulator (without any symmetry constraint) was constructed by Haldane.¹ With periodic boundary conditions, it has two single-particle Bloch bands separated by a gap Δ . Its nontrivial topological invariant is a non-vanishing Chern number that is proportional to the Hall conductivity.² This example is a representative of topological band insulators called Chern insulators. In open geometries, Chern insulators support gapless single-particle boundary states, i.e., edge states. These edge states are chiral in that they propagate along the edge either clockwise or anti-clockwise depending on the sign taken by the Hall conductivity of the occupied bands. Since intra-edge backward scattering is not permitted, these chiral edge states are robust to perturbations.³

A more intricate example of a strong two-dimensional topological band insulator was constructed by Kane and Mele.^{4,5} With periodic boundary conditions, it has four single-particle bands that form two Kramers' pairs of

bands as a consequence of time-reversal symmetry. However, spin-rotation symmetry is completely broken by spin-orbit coupling. A gap Δ separates the two pairs of bands, and the Bloch wave functions of the occupied bands have a nontrivial topological \mathbb{Z}_2 index.⁵ In an open geometry, there is a Kramers' pair of edge states, called helical edge states (Fig. 1). This pair is robust to perturbations that respect the time-reversal symmetry.⁶⁻⁸ This example is a representative of topological band insulators called \mathbb{Z}_2 topological band insulators.

Weak topological band insulators are built out of strong lower-dimensional topological band insulators. For example, a weak three-dimensional topological insulator can be a stack of strong two-dimensional topological insulators as is illustrated in Fig. 2. Weak topological band insulators can support surface states in open geometries that are inherited from the boundary states of their lower-dimensional strong topological band building blocks.

Weak three-dimensional Chern insulators have been studied theoretically in the context of three-dimensional generalizations of the quantum Hall effect.⁹⁻¹⁶ Two-dimensional transport at the surface of GaAs/AlGaAs multilayer structures subjected to a large uniform magnetic field parallel to the stacking axis was established in Ref. 17.

Models for weak three-dimensional \mathbb{Z}_2 topological band insulators were constructed simultaneously with models for strong three-dimensional \mathbb{Z}_2 topological insulators.¹⁸⁻²¹ Of course, most of the excitement generated by these works was reserved for the strong three-

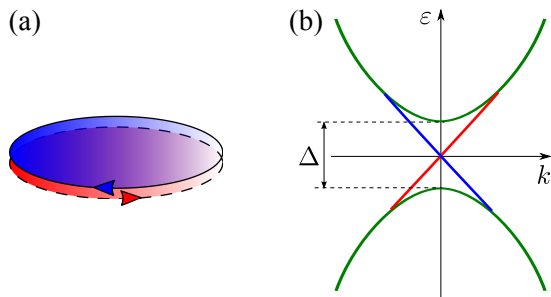


FIG. 1. (Color online:) Cartoon representation of a strong two-dimensional \mathbb{Z}_2 topological band insulator with one connected boundary. (a) Electrons are noninteracting and confined within an ellipse in two-dimensional position space. A single pair of counter propagating helical edge states at zero energy are denoted by the thick and dashed lines with arrows along the connected boundary of the ellipse, respectively. They are confined to this one-dimensional boundary. (b) The single-particle spectrum consists of eigenstates separated by an energy gap Δ and eigenstates crossing the band gap Δ . The former eigenstates are the bulk eigenstates. The latter eigenstates are the edge eigenstates. The momentum k is the momentum along the boundary. The wave functions in position space of bulk eigenstates are supported in the shaded region of the ellipse. The wave functions in position space of edge eigenstates are extended along the edge and labeled by the momentum quantum number k along the edge, while they decay exponentially fast away from the edge.

dimensional \mathbb{Z}_2 topological insulators, especially after their experimental discovery in $\text{Bi}_{1-x}\text{Sb}_x$,²² Bi_2Se_3 ,^{23,24} and TlBiSe_2 .^{25–28} A weak three-dimensional \mathbb{Z}_2 topological insulator has been identified experimentally in the form of $\text{Bi}_{14}\text{Rh}_3\text{I}_9$.²⁹

Two-dimensional surfaces of strong (weak) three-dimensional \mathbb{Z}_2 topological band insulators support an odd (even) number of helical surface states. Each such helical surface state effectively realizes the linear dispersion of a massless two-component Dirac particle in two-dimensional momentum space. A single massless two-component Dirac particle cannot accommodate a mass term without breaking time-reversal symmetry in two dimensions. In this sense, a single Dirac cone on the surface of a strong three-dimensional \mathbb{Z}_2 topological band insulator is protected by time-reversal symmetry. This is not so for a pair of massless two-component Dirac particles in two dimensions. They can accommodate a mass term that does not break time-reversal symmetry, but breaks some of the lattice symmetries. Thus, a pair of Dirac cones on the surface of a weak \mathbb{Z}_2 topological band insulator is not protected by time-reversal symmetry.¹⁸ For this reason, weak topological band insulators have initially attracted less interest than strong topological band insulators.

In the presence of disorder that preserves the time-reversal symmetry, momentum is not a good quantum number anymore. In fact, the very notion of a spectral gap or of gaplessness is meaningless in the presence of

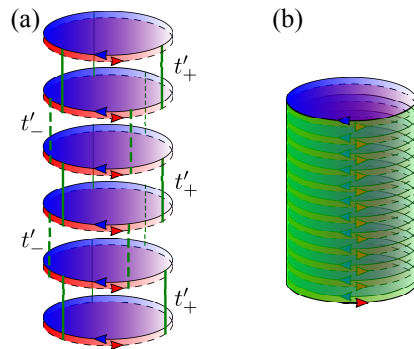


FIG. 2. (Color online:) (a) Cartoon representation of a weak layered \mathbb{Z}_2 topological band insulator with open boundary conditions along the layering axis. A vertical line represents the amplitude for the Kramers' degenerate helical edge states of a layer consisting of a strong two-dimensional \mathbb{Z}_2 topological band insulator to hop to one of its adjacent layers. The vertical lines are alternatively drawn with solid and dotted lines in order to indicate that the magnitude of this hopping amplitude takes two distinct values. As a consequence of the breaking of translation invariance by one lattice spacing along the stacking axis, a dimerization gap opens for all helical edge states, i.e., for all surface states of this weak layered \mathbb{Z}_2 topological band insulator. (b) The topology in (a) is that of a cylinder.

disorder. It is replaced by the notion of mobility edges that defines the windows of single-particle energies for which single-particle states are localized by disorder.

The consequences of disorder weaker than the bulk band gap Δ for the surface states of a strong three-dimensional \mathbb{Z}_2 topological band insulator can be accounted for by describing the helical surface states as massless two-component Dirac fermions in two-dimensional space perturbed by local potentials that break translation invariance along the boundary but preserve time-reversal symmetry. In turn, this effective field theory can be approximated by a nonlinear σ -model (NL σ M) with a two-dimensional base space and a target space determined by the symplectic symmetry of the effective Hamiltonian, that is augmented by a topological term.^{30,31} This topological term prevents the transition from a conducting to an insulating phase as the disorder strength on the boundary is made arbitrarily large,³² as is implied by the strictly monotonic one-parameter scaling law obeyed by the conductivity σ on a surface of area L^2 that is captured by the beta function $d\ln\sigma/d\ln L$ shown in Fig. 3.^{33,34} By contrast, no topological term augments the NL σ M description of the effect of time-reversal-symmetric disorder for the surface states of a weak three-dimensional \mathbb{Z}_2 topological band insulator.³¹ One might be tempted to deduce from this fact that strong disorder always causes localization. This is not so however.

The even number of Dirac points on the surface of a weak three-dimensional \mathbb{Z}_2 topological band insulator allows a time-reversal symmetric perturbation, a dimer-

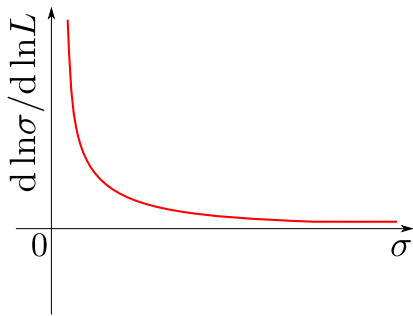


FIG. 3. (Color online:) Qualitative beta function $d \ln \sigma / d \ln L$ for the conductivity σ of a massless two-component Dirac fermion on the surface with the area L^2 of a strong three-dimensional \mathbb{Z}_2 topological insulator, when subjected to disorder that preserves time-reversal symmetry. The beta function $d \ln \sigma / d \ln L$ is deduced from the numerics of Refs. 33 and 34. It is always positive and the smaller the initial value of the conductivity is the larger the positive value of the beta function.

ization, to open a spectral gap $2|m| \ll \Delta$ for the surface states at the cost of breaking some lattice symmetries.^{18,35} The effective Dirac Hamiltonian with a dimerization mass m in the clean limit turns out to be the one describing two-dimensional strong \mathbb{Z}_2 topological insulators.^{35–38} Hence, the sign of the mass m selects one of the two topologically distinct massive phases of a strong two-dimensional \mathbb{Z}_2 topological band insulator. The surface Dirac points can thus be associated with a quantum critical point separating two massive dimer phases with less lattice symmetries. By the Callan-Harvey effect,³⁹ a defect of the dimerization mass m along a curve on the surface of the weak three-dimensional \mathbb{Z}_2 topological band insulator at which m smoothly changes sign binds a pair of Kramers degenerate helical edge states whose dispersion crosses the gap $2|m|$ of the surface states.^{35–38} Provided the disorder is time-reversal symmetric, this quantum critical point has the remarkable property that, perturbed by time-reversal symmetric surface disorder, it turns into a metallic phase separating two insulating dimerized phases.

This counter-intuitive conclusion was first reached by Ringel, Kraus, and Stern for a layered model of a weak three-dimensional \mathbb{Z}_2 topological band insulator based on the sensitivity to twisted boundary condition of spectral flows.⁴⁰ Mong, Bardarson, and Moore did a numerical study of the disordered Dirac equation capturing the low-energy and long-wave-length limit of the disordered surface states of a weak three-dimensional \mathbb{Z}_2 topological band insulator that confirmed this prediction and, furthermore, showed that the clean Dirac critical point is smoothly connected to a metallic phase as shown in Fig. 4.³⁶ Fu and Kane pointed out the importance of \mathbb{Z}_2 vortices in a description in terms of a NL σ M of disordered surface states of a weak three-dimensional \mathbb{Z}_2 topological band insulator.³⁷ Furthermore, they have proposed the possibility of a non-monotonous renormalization-group

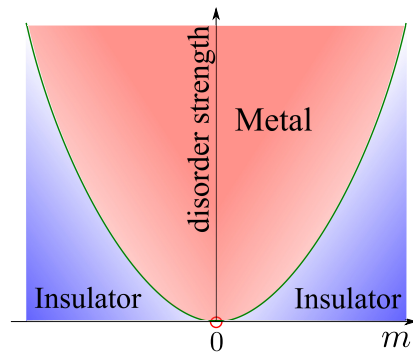


FIG. 4. (Color online:) Phase diagram from Ref. 36 for the surface states of a weak three-dimensional \mathbb{Z}_2 topological band insulator as a function of the mass that opens a band gap at the Dirac points (horizontal axis) and the disorder strength (vertical axis). It is assumed that the disorder does not mix surface states localized on disconnected boundaries of the three-dimensional \mathbb{Z}_2 topological band insulator.³² The origin of the phase diagram is the critical point corresponding to an even number of two-component massless Dirac fermions at their Dirac point.

flow on the line $m = 0$ in Fig. 4. However, the monotonic scaling observed in Ref. 36 seems to indicate that $d \ln \sigma / d L > 0$ at $m = 0$, as is the case of surface states of a strong \mathbb{Z}_2 topological insulator shown in Fig. 3. Finally, a numerical study of the localization properties of a disordered lattice model for a three-dimensional \mathbb{Z}_2 topological band insulator that interpolates from the strong to the weak regimes is consistent with the phase diagram of Fig. 4.⁴¹

A question that has been left open so far is that of the nature of the phase transition between the insulating and the metallic phases in Fig. 4. In this paper, we construct a two-dimensional network model for the surface states of a weak three-dimensional \mathbb{Z}_2 topological band insulator. We call this network model the two-dimensional spin-directed \mathbb{Z}_2 network model. It differs from a two-dimensional \mathbb{Z}_2 network model that we constructed in Ref. 42 to study the effects of disorder on the phase diagram of a strong two-dimensional \mathbb{Z}_2 topological band insulator.^{43,44} For the two-dimensional spin-directed \mathbb{Z}_2 network model, we argue by considering several limiting cases and by mapping it to effective Dirac Hamiltonians that, without dimerization, there is no insulating phase even when disorder is strong. With a finite dimerization, we establish numerically the existence of three phases, two insulating phases that are separated by a metallic phase. We show that, aside from being continuous, the quantum phase transition between the insulating and metallic phases belongs to the two-dimensional universality class with symplectic symmetry within the theory of Anderson localization, irrespectively of whether the insulating phases are topologically trivial or nontrivial.

The paper is organized as follows. The two-dimensional spin-directed \mathbb{Z}_2 network model that de-

scribes the combined effects of dimerization and disorder for the surface states of a weak three-dimensional \mathbb{Z}_2 band insulator is constructed in Sec. II. This model is studied in Sec. III, in which the main numerical results of this paper are explained. Section IV is devoted to the two-dimensional spin-directed \mathbb{Z}_2 network model that describes the combined effects of trimerization and disorder on the surface states of a weak three-dimensional \mathbb{Z}_2 band insulator. Section V closes the paper by summarizing our results. We also present in two Appendices the relationship between the model from Sec. II A captured by Fig. 2, the two-dimensional spin-directed \mathbb{Z}_2 network model from Sec. II B, and two-dimensional Dirac fermions. Thereby, we establish the complementarity of our results to those from Ref. 36. A detailed presentation of our finite-size scaling analysis is given in Ref. 55.

II. DEFINITIONS AND MAIN RESULTS

A. Quasi-one-dimensional model for the surface states of a weak three-dimensional \mathbb{Z}_2 topological insulator

We start from the model of a weak three-dimensional \mathbb{Z}_2 topological band insulator that is depicted in Fig. 2. It consists of a stacking of layers, each of which represents a strong two-dimensional \mathbb{Z}_2 topological band insulator depicted in Fig. 1(a). We assume that all pancakes in Fig. 2(a) are identical. The single-particle spectrum corresponding to any pancake in Fig. 2(a) is shown in Fig. 1(b). It consists of two continua corresponding to bulk single-particle eigenstates separated by the band gap Δ and of a pair of Kramers' degenerate helical edge states crossing the bulk gap. We will always assume that Δ is much larger than the amplitude $\max\{|t'_-|, |t'_+|\}$ for edge states on adjacent pancakes to hop between layers. Here, t'_+ is depicted by a solid line in Fig. 2, while t'_- is drawn as a dotted line in Fig. 2. The characteristic energy

$$\delta' := +\sqrt{\frac{|t'^2_+ - t'^2_-|}{2}} \quad (2.1a)$$

quantifies the amount by which translation symmetry by one stacking layer is broken, i.e., the amount of dimerization about the average hopping amplitude

$$t' := +\sqrt{\frac{t'^2_+ + t'^2_-}{2}}. \quad (2.1b)$$

The hierarchy of energy scales

$$\Delta \gg t' \geq \delta' \quad (2.1c)$$

will be assumed.

Assumption (2.1c) justifies ignoring the degrees of freedom from the bulk altogether and keeping only the degrees of freedom living on the edges of Fig. 2 for ener-

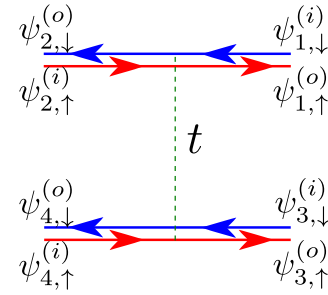


FIG. 5. (Color online:) An elementary scattering event in the spin-directed \mathbb{Z}_2 network model maps four incoming plane waves into four outgoing plane waves through a unitary 4×4 matrix S compatible with the operation of time reversal. By demanding that the operation of time reversal is an antiunitary operation that squares to minus the 4×4 identity matrix, the scattering matrix S can break spin-rotation symmetry (hence the spin labels on the plane waves), but preserves time-reversal symmetry. In other words, the scattering matrix belongs to the symplectic class of scattering matrices. The matrix S is represented by Eq. (2.3).

gies below Δ . In Appendix A, we present a quasi-one-dimensional Hamiltonian that governs the dynamics of the surface states of Fig. 2 when

$$\Delta \gg t' \gg \delta'. \quad (2.2)$$

This approach is inspired from similar constructions when time-reversal symmetry is broken (see Refs. 45–48). We show in Appendix A, that there exists a continuum limit along the stacking axis that reduces this effective Hamiltonian to the Dirac Hamiltonian studied numerically by Mong, Bardarson, and Moore in Ref. 36.

B. Two-dimensional spin-directed \mathbb{Z}_2 network model for the surface states of a weak three-dimensional \mathbb{Z}_2 topological insulator

Alternatively, we may encode the dynamics of the surface states of Fig. 2, under the assumption that the hierarchy of energy scales (2.1c) holds, in terms of the unitary scattering matrix of a two-dimensional spin-directed \mathbb{Z}_2 network model.

The elementary building block of the two-dimensional spin-directed \mathbb{Z}_2 network model is a 4×4 unitary matrix S that scatters 4 incoming plane waves into four outgoing plane waves. The conventions on the labels of the scattering states that we choose to represent S are defined in Fig. 5. If we demand that this 4×4 unitary matrix S preserves time-reversal symmetry, whereby time reversal is represented by an antiunitary map on scattering states that squares to minus the 4×4 unit matrix, we obtain

the representation

$$\begin{pmatrix} \psi_{1,\uparrow}^{(o)} \\ \psi_{2,\downarrow}^{(o)} \\ \psi_{3,\uparrow}^{(o)} \\ \psi_{4,\downarrow}^{(o)} \end{pmatrix} = S \begin{pmatrix} \psi_{2,\uparrow}^{(i)} \\ \psi_{1,\downarrow}^{(i)} \\ \psi_{4,\uparrow}^{(i)} \\ \psi_{3,\downarrow}^{(i)} \end{pmatrix}, \quad (2.3a)$$

where the scattering matrix that maps four incoming into four outgoing plane waves has the 2×2 block structure

$$S := e^{+i\phi_0} \begin{pmatrix} r e^{+i\phi_3} \sigma_0 & t Q \\ -t Q^\dagger & r e^{-i\phi_3} \sigma_0 \end{pmatrix}. \quad (2.3b)$$

The real numbers r and t obey the condition

$$1 = r^2 + t^2 \iff r = \tanh x, \quad t = \frac{1}{\cosh x}, \quad x \in \mathbb{R}, \quad (2.3c)$$

and may be interpreted as the reflection and transmission amplitudes, respectively, upon inspection of the transformation laws of the labels 1 and 2 on the one hand and 3 and 4 on the other hand from Fig. 5. The 2×2 matrix Q is defined by

$$\begin{aligned} Q &= \begin{pmatrix} e^{+i\phi_1} \cos \theta & e^{+i\phi_2} \sin \theta \\ e^{-i\phi_2} \sin \theta & -e^{-i\phi_1} \cos \theta \end{pmatrix} \\ &= i \sin \phi_1 \cos \theta \sigma_0 + \cos \phi_2 \sin \theta \sigma_1 \\ &\quad - \sin \phi_2 \sin \theta \sigma_2 + \cos \phi_1 \cos \theta \sigma_3. \end{aligned} \quad (2.3d)$$

It acts on the spin up and down labels of the incoming and outgoing plane waves through the unit 2×2 matrix σ_0 and the three Pauli matrices σ_1 , σ_2 , and σ_3 . The parameter $0 \leq \theta \leq \pi/2$ quantifies the amount of spin-rotation symmetry breaking. When $\theta = 0$, the $SU(2)$ spin-rotation symmetry is broken down to the subgroup $U(1)$. Any $0 < \theta \leq \pi/2$ breaks the residual $U(1)$ symmetry by a spin-flip process. The rate of this spin-flip tunneling is maximal for $\theta = \pi/2$. The remaining four phases ϕ_j ($0 \leq \phi_j < 2\pi$, $j = 0, 1, 2, 3$) parametrize the phase arbitrariness of incoming and outgoing plane waves compatible with the condition

$$\begin{pmatrix} \sigma_2 & 0 \\ 0 & \sigma_2 \end{pmatrix} S^* \begin{pmatrix} \sigma_2 & 0 \\ 0 & \sigma_2 \end{pmatrix} = S^\dagger \quad (2.3e)$$

that implements time-reversal symmetry on the scattering matrix. The sign of the amplitudes t and r can always be absorbed into the shifts $\phi_{1,2} \rightarrow \phi_{1,2} + \pi$ and $\phi_3 \rightarrow \phi_3 + \pi$, respectively. Hence, we may assume without loss of generality that t and r are positive numbers.

A two-dimensional spin-directed \mathbb{Z}_2 network model is defined by arranging a collection of elementary scattering events, with possibly distinct values for the parameters t , θ , ϕ_j ($j = 0, 1, 2, 3$), as is shown in Fig. 6. These network models are spin-directed because, if all transmission amplitudes are chosen to vanish, there is no flipping of the spin quantum numbers so that there are M independent pairs of Kramers' degenerate helical edge states propagating unimpeded along M one-dimensional channels.

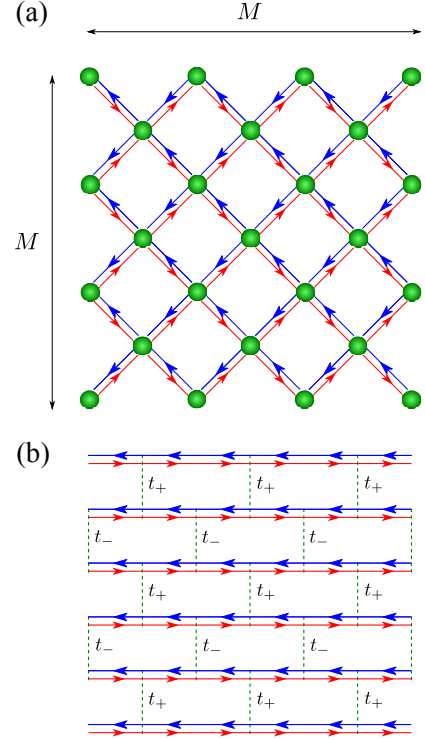


FIG. 6. (Color online:) A two-dimensional spin-directed \mathbb{Z}_2 network model built out of the elementary scattering processes shown in Fig. 5 in the vertex (a) and the brick-wall representations (b), respectively. The red and blue lines represent the flow of electrons with up and down spins, respectively. The geometrical dimension of both networks in (a) and (b) is $M \times M$ with $M = 6$. In both representations, one M counts the number of pairs of up and down spins that move from left to right or right to left, while the other M counts the number of pairs of up and down spins that move from up to down or down to up. In the brick-wall representation, each dotted line represents an elementary scattering shown in Fig. 5 with the transmission amplitude t_+ or t_- . This periodic pattern implements one of two dimerization patterns, the other one following from interchanging t_+ and t_- .

The two-dimensional spin-directed \mathbb{Z}_2 network model is thus different from the two-dimensional (undirected) \mathbb{Z}_2 network model that realizes strong two-dimensional \mathbb{Z}_2 topological insulators studied in Refs. 42–44, as can be verified by comparing Fig. 6 to Fig. 7. In the two-dimensional (undirected) \mathbb{Z}_2 network model, the nodes labeled by r in Fig. 7 are obtained from those labeled by t through a 90 degree rotation. Hence, the two-dimensional (undirected) \mathbb{Z}_2 network model is invariant (on average) under 90 degree rotation, whereas there is no discrete rotation symmetry for the two-dimensional spin-directed \mathbb{Z}_2 network model.

Disorder is introduced in any two-dimensional spin-directed \mathbb{Z}_2 network model by choosing the four phases ϕ_j ($j = 0, 1, 2, 3$) of any elementary scattering process making up a network model to be random numbers independently and identically distributed with a uniform

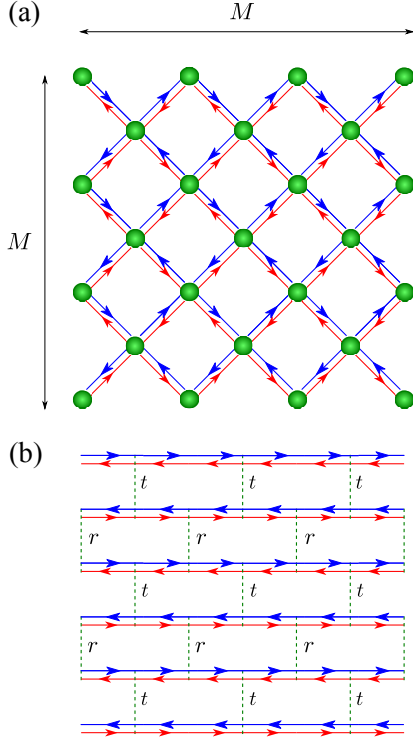


FIG. 7. (Color online:) The two-dimensional \mathbb{Z}_2 network model studied in Refs. 42, 43, and 44 for a strong two-dimensional \mathbb{Z}_2 topological insulator with $M = 6$ in the vertex (a) and the brick-wall representations (b), respectively. Note that the flow direction of the same spin component (up or down) is opposite on adjacent layers in (b), in contrast to Fig. 6(b).

distribution on the interval

$$\left[-\frac{\delta\phi}{2}, +\frac{\delta\phi}{2} \right]. \quad (2.4)$$

In this paper, we study the combined effects of dimerization and disorder on the two-dimensional spin-directed \mathbb{Z}_2 network model. To incorporate dimerization, we assume that the squared amplitude of the transmission (reflection) amplitude alternates in a periodic fashion between the two values labeled by \pm of

$$0 \leq t_{\pm}^2 \leq 1 \quad (r_{\pm}^2 = 1 - t_{\pm}^2), \quad (2.5a)$$

where

$$t_{\pm}^2 := \begin{cases} t^2 \pm \delta^2, & \text{if } t_+^2 > t_-^2, \\ t^2 \mp \delta^2, & \text{if } t_+^2 < t_-^2. \end{cases} \quad (2.5b)$$

Equation (2.5b) emphasizes that the choice of which of the squared transmission amplitudes t_+^2 and t_-^2 is the largest is arbitrary for an alternating covering of the network. When $\delta = 0$, there is no dimerization. Parameter space Ω_{4d} for the two-dimensional spin-directed \mathbb{Z}_2

network model with disorder and dimerization is four-dimensional. We choose the parametrization

$$\Omega_{4d} = \Omega_{4d}^+ \cup \Omega_{4d}^- \quad (2.6a)$$

with

$$\Omega_{4d}^{\pm} := \left\{ (t^2, \theta, \delta\phi, \pm\delta^2) \mid t^2 \in [0, 1], \theta \in [0, \pi/2], \right. \\ \left. \delta\phi \in [0, 2\pi[, \delta^2 \in [0, 1], 0 \leq t^2 + \delta^2 \leq 1 \right\}. \quad (2.6b)$$

However, we will choose the disorder to be maximal in that

$$\delta\phi = 2\pi. \quad (2.7a)$$

If so, parameter space is three-dimensional and given by

$$\Omega_{3d} = \Omega_{3d}^+ \cup \Omega_{3d}^- \quad (2.7b)$$

with

$$\Omega_{3d}^{\pm} := \left\{ (t^2, \theta, \pm\delta^2) \mid t^2 \in [0, 1], \theta \in [0, \pi/2], \right. \\ \left. \delta^2 \in [0, 1], 0 \leq t^2 + \delta^2 \leq 1 \right\}. \quad (2.7c)$$

The interchange of t_+^2 and t_-^2 amounts to the interchange of Ω_{xd}^+ and Ω_{xd}^- (here either $x = 4$ or $x = 3$).

We show in Appendix B that there exists two continuum limits of the two-dimensional spin-directed \mathbb{Z}_2 network model in the vicinity, as measured by a small δ^2 , of the lines $\theta = \pi/2$ with t^2 arbitrary and $\theta = 0$ with t^2 arbitrary, respectively. The line with $\theta = \pi/2$ delivers the Dirac Hamiltonian studied numerically by Mong, Bardarson, and Moore in Ref. 36.

C. Some limiting cases without dimerization

There are several lines in the two-dimensional subspace

$$(t^2, \theta, \delta^2 = 0) \in [0, 1] \times [0, \pi/2] \quad (2.8)$$

of the parameter space (2.7) without dimerization for which the two-dimensional spin-directed \mathbb{Z}_2 network model simplifies.

1. Limit $t^2 = 0$ without dimerization

We set

$$\delta^2 = t^2 = 0. \quad (2.9)$$

When $t^2 = 0$, the elementary scattering matrix from Eq. (2.3) is block diagonal and independent of θ ,

$$S = e^{+i\phi_0} \begin{pmatrix} e^{+i\phi_3} \sigma_0 & 0 \\ 0 & e^{-i\phi_3} \sigma_0 \end{pmatrix}. \quad (2.10)$$

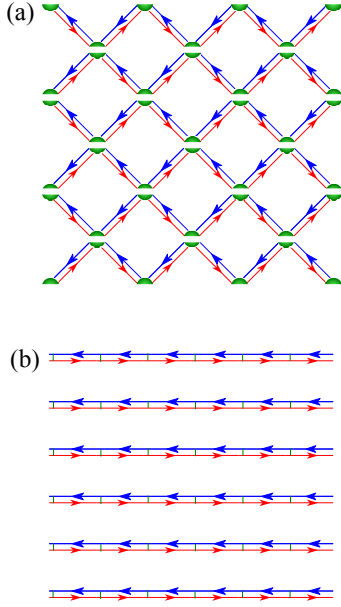


FIG. 8. (Color online:) When $\delta^2 = t^2 = 0$, the two-dimensional spin-directed \mathbb{Z}_2 network model from Fig. 6 decouples into M one-dimensional channels, each of which consists of a single Kramers' degenerate pair of helical edge states that propagate unimpeded by the disorder. Panels (a) and (b) are drawn using the vertex and the brick-wall representations, respectively.

The two-dimensional spin-directed \mathbb{Z}_2 model of Fig. 6 is shown in Fig. 8 when $\delta^2 = t^2 = 0$. It represents M decoupled one-dimensional channels, each of which consists of a Kramers' degenerate pair of helical edge states that propagates unimpeded by the disorder. The localization length is infinite in the direction of propagation of these helical edge states, while it is vanishing in the orthogonal direction. The fixed point (2.9) is thus the *quasi-one-dimensional symplectic metallic fixed point*.

2. Limit $\theta = 0$ without dimerization

We set

$$\delta^2 = \theta = 0. \quad (2.11)$$

Since θ measures in dimensionless units the characteristic strength of spin-orbit interactions with the convention that the Rashba-like spin-orbit coupling vanishes when $\theta = 0$, the spin-directed \mathbb{Z}_2 network model with $\delta^2 = \theta = 0$ is expected to decouple into two two-dimensional directed Chalker-Coddington (CC) models,¹⁰ one for the spin-up and one for the spin down plane waves, that are related by time-reversal symmetry. This decoupling is shown in Fig. 9. In a two-dimensional directed CC network model,^{9–16} propagation is uni-directional along the horizontal direction and bi-directional along the vertical direction of the two-dimensional network.

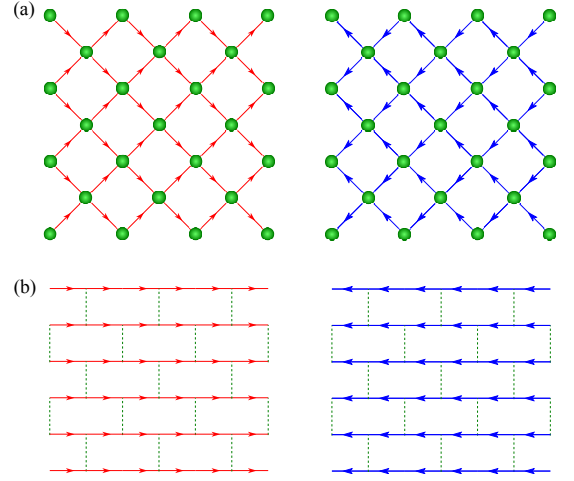


FIG. 9. (Color online:) When $\delta^2 = \theta = 0$, the two-dimensional spin-directed \mathbb{Z}_2 network model from Fig. 6 decouples into two directed CC models that are related by time reversal. Panels (a) and (b) are drawn using the vertex and the brick-wall representations, respectively.

To establish this decoupling at $\theta = 0$, we start from

$$\begin{pmatrix} \psi_{1,\uparrow}^{(o)} \\ \psi_{2,\downarrow}^{(o)} \\ \psi_{3,\uparrow}^{(o)} \\ \psi_{4,\downarrow}^{(o)} \end{pmatrix} = S \begin{pmatrix} \psi_{2,\uparrow}^{(i)} \\ \psi_{1,\downarrow}^{(i)} \\ \psi_{4,\uparrow}^{(i)} \\ \psi_{3,\downarrow}^{(i)} \end{pmatrix}, \quad (2.12a)$$

where S takes the limiting form

$$S = e^{+i\phi_0} \begin{pmatrix} r e^{+i\phi_3} \sigma_0 & +tQ \\ -tQ^\dagger & +r e^{-i\phi_3} \sigma_0 \end{pmatrix} \quad (2.12b)$$

with the 2×2 diagonal block

$$Q = \begin{pmatrix} +e^{+i\phi_1} & 0 \\ 0 & -e^{-i\phi_1} \end{pmatrix}. \quad (2.12c)$$

It is then advantageous for our purpose to do a unitary transformation that renders explicit the reducibility of the scattering matrix (2.12) in the spin degrees of freedom,

$$\begin{pmatrix} \psi_{1,\uparrow}^{(o)} \\ \psi_{3,\uparrow}^{(o)} \\ \psi_{2,\downarrow}^{(o)} \\ \psi_{4,\downarrow}^{(o)} \end{pmatrix} = \tilde{S} \begin{pmatrix} \psi_{2,\uparrow}^{(i)} \\ \psi_{4,\uparrow}^{(i)} \\ \psi_{1,\downarrow}^{(i)} \\ \psi_{3,\downarrow}^{(i)} \end{pmatrix}, \quad (2.13a)$$

where \tilde{S} takes the limiting form

$$\tilde{S} = e^{+i\phi_0} \begin{pmatrix} \tilde{Q}(t, \phi_1, \phi_3) & 0 \\ 0 & \tilde{Q}^T(t, \phi_1, \phi_3) \end{pmatrix} \quad (2.13b)$$

with the 2×2 block

$$\tilde{Q}(t, \phi_1, \phi_3) = \begin{pmatrix} +r e^{+i\phi_3} & +t e^{+i\phi_1} \\ -t e^{-i\phi_1} & +r e^{-i\phi_3} \end{pmatrix}. \quad (2.13c)$$

The upper-left and lower-right 2×2 blocks $e^{+i\phi_0} \tilde{Q}(t, \phi_1, \phi_3)$ and $e^{+i\phi_0} \tilde{Q}^T(t, \phi_1, \phi_3)$, respectively, are related by time reversal. Each block defines the elementary scattering matrix of the two-dimensional directed CC network model.¹⁰ It is shown in Ref. 10 (see also Refs. 9 and 11–16) that the localization properties of the two-dimensional directed CC network model are the following. Transport is highly anisotropic, for it is perfect along one direction and critical along the orthogonal direction of the two-dimensional network.⁴⁹ The fixed point (2.11) is thus the *spin-chiral metallic fixed point*.

3. Limit $r^2 = 0$ without dimerization

We set

$$\delta^2 = r^2 = 0. \quad (2.14)$$

When $r^2 = 0$, the elementary scattering matrix from Eq. (2.3) becomes

$$\begin{pmatrix} \psi_{1,\uparrow}^{(o)} \\ \psi_{2,\downarrow}^{(o)} \\ \psi_{3,\uparrow}^{(o)} \\ \psi_{4,\downarrow}^{(o)} \end{pmatrix} = S \begin{pmatrix} \psi_{2,\uparrow}^{(i)} \\ \psi_{1,\downarrow}^{(i)} \\ \psi_{4,\uparrow}^{(i)} \\ \psi_{3,\downarrow}^{(i)} \end{pmatrix}, \quad (2.15a)$$

where S takes the limiting form

$$S = e^{+i\phi_0} \begin{pmatrix} 0 & +Q(\theta, \phi_1, \phi_2) \\ -Q^\dagger(\theta, \phi_1, \phi_2) & 0 \end{pmatrix} \quad (2.15b)$$

with the 2×2 block

$$Q(\theta, \phi_1, \phi_2) = \begin{pmatrix} +e^{+i\phi_1} \cos \theta & +e^{+i\phi_2} \sin \theta \\ +e^{-i\phi_2} \sin \theta & -e^{-i\phi_1} \cos \theta \end{pmatrix}. \quad (2.15c)$$

We do the unitary transformation

$$\begin{pmatrix} \psi_{1,\uparrow}^{(o)} \\ \psi_{2,\downarrow}^{(o)} \\ \psi_{3,\uparrow}^{(o)} \\ \psi_{4,\downarrow}^{(o)} \end{pmatrix} = \tilde{S} \begin{pmatrix} \psi_{3,\downarrow}^{(i)} \\ \psi_{4,\uparrow}^{(i)} \\ \psi_{1,\downarrow}^{(i)} \\ \psi_{2,\uparrow}^{(i)} \end{pmatrix}, \quad (2.16a)$$

where \tilde{S} takes the limiting form

$$\tilde{S} = e^{+i\phi_0} \begin{pmatrix} \tilde{Q}(\cos \theta, \phi_1, \phi_2) & 0 \\ 0 & \tilde{Q}^T(\cos \theta, \phi_1, \phi_2 + \pi) \end{pmatrix} \quad (2.16b)$$

with the 2×2 block

$$\tilde{Q}(\cos \theta, \phi_1, \phi_2) = \begin{pmatrix} +e^{+i\phi_2} \sin \theta & +e^{+i\phi_1} \cos \theta \\ -e^{-i\phi_1} \cos \theta & +e^{-i\phi_2} \sin \theta \end{pmatrix}. \quad (2.16c)$$

The upper-left and lower-right 2×2 blocks $e^{+i\phi_0} \tilde{Q}(\cos \theta, \phi_1, \phi_2)$ and $e^{+i\phi_0} \tilde{Q}^T(\cos \theta, \phi_1, \phi_2 + \pi)$, respectively, are related by time reversal.

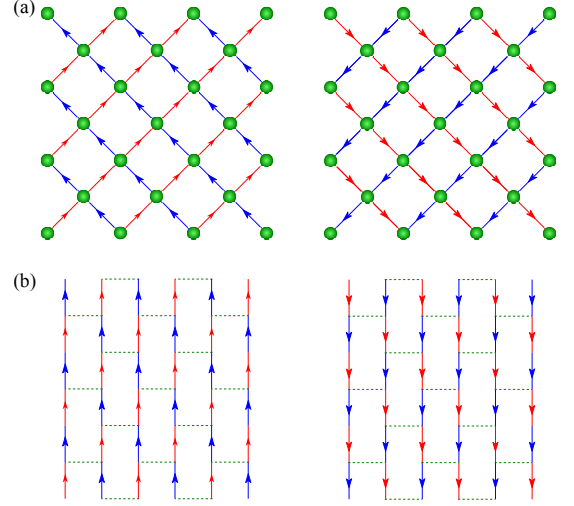


FIG. 10. (Color online:) When $\delta^2 = r^2 = 0$, the two-dimensional spin-directed \mathbb{Z}_2 network model from Fig. 6 decouples into two directed CC models that are related by time reversal. Panels (a) and (b) are drawn using the vertex and the brick-wall representations, respectively.

The elementary scattering matrix (2.16) is identical to the elementary scattering matrix (2.13) as implied by the identifications

$$\sin \theta \rightarrow r, \quad \cos \theta \rightarrow t, \quad \phi_2 \rightarrow \phi_3. \quad (2.17)$$

Consequently, the two-dimensional directed \mathbb{Z}_2 network model from Fig. 6 decouples into two directed CC network models that are related by time reversal when $\delta^2 = r^2 = 0$. This decoupling is shown in Fig. 10. Transport is highly anisotropic, for it is perfect along one spanning vector and critical along the second spanning vector of the two-dimensional network. The fixed point (2.14) is thus again the *spin-chiral metallic fixed point*. The relationship between the fixed points (2.14) and (2.11) is that the directions for perfect and critical transport have been interchanged.

4. Limit $\theta = \pi/2$ without dimerization

We set

$$\delta^2 = \theta - \frac{\pi}{2} = 0. \quad (2.18)$$

When $\theta = \pi/2$, the elementary scattering matrix from Eq. (2.3) becomes

$$\begin{pmatrix} \psi_{1,\uparrow}^{(o)} \\ \psi_{2,\downarrow}^{(o)} \\ \psi_{3,\uparrow}^{(o)} \\ \psi_{4,\downarrow}^{(o)} \end{pmatrix} = S \begin{pmatrix} \psi_{2,\uparrow}^{(i)} \\ \psi_{1,\downarrow}^{(i)} \\ \psi_{4,\uparrow}^{(i)} \\ \psi_{3,\downarrow}^{(i)} \end{pmatrix}, \quad (2.19a)$$

where S takes the limiting form

$$S = e^{+i\phi_0} \begin{pmatrix} +r e^{+i\phi_3} \sigma_0 & +t Q \\ -t Q^\dagger & +r e^{-i\phi_3} \sigma_0 \end{pmatrix} \quad (2.19b)$$

with the 2×2 block

$$Q = \begin{pmatrix} 0 & e^{+i\phi_2} \\ e^{-i\phi_2} & 0 \end{pmatrix}. \quad (2.19c)$$

We do the unitary transformation

$$\begin{pmatrix} \psi_{1,\uparrow}^{(o)} \\ \psi_{4,\downarrow}^{(o)} \\ \psi_{2,\downarrow}^{(o)} \\ \psi_{3,\uparrow}^{(o)} \end{pmatrix} = \tilde{S} \begin{pmatrix} \psi_{2,\uparrow}^{(i)} \\ \psi_{3,\downarrow}^{(i)} \\ \psi_{1,\downarrow}^{(i)} \\ \psi_{4,\uparrow}^{(i)} \end{pmatrix}, \quad (2.20a)$$

where \tilde{S} takes the limiting form

$$\tilde{S} = e^{+i\phi_0} \begin{pmatrix} \tilde{Q}(t, \phi_2, \phi_3) & 0 \\ 0 & \tilde{Q}^T(t, \phi_2 + \pi, \phi_3) \end{pmatrix} \quad (2.20b)$$

with

$$\tilde{Q}(t, \phi_2, \phi_3) = \begin{pmatrix} +r e^{+i\phi_3} & +t e^{+i\phi_2} \\ -t e^{-i\phi_2} & +r e^{-i\phi_3} \end{pmatrix}. \quad (2.20c)$$

The upper-left and lower-right 2×2 blocks $e^{+i\phi_0} \tilde{Q}(t, \phi_2, \phi_3)$ and $e^{+i\phi_0} \tilde{Q}^T(t, \phi_2 + \pi, \phi_3)$, respectively, are related by time reversal. Moreover, they are nothing but the elementary scattering matrix for the two-dimensional CC network model that describes the localization properties of the lowest Landau level perturbed by disorder in the integer quantum Hall effect (IQHE). Consequently, the two-dimensional spin-directed \mathbb{Z}_2 network model from Fig. 6 decouples into two CC network models that are related by time reversal when $\delta^2 = \theta - \pi/2 = 0$. This decoupling is shown in Fig. 11.

Chalker and Coddington showed in Ref. 50 that the CC network model is critical if every node of the network is described by the scattering matrix $e^{+i\phi_0} \tilde{Q}(t, \phi_2, \phi_3)$ given in Eq. (2.20c) sharing the same tunneling amplitude t . Hence, the two-dimensional spin-directed \mathbb{Z}_2 network model with $\delta^2 = \theta - \pi/2 = 0$ is always critical. In the special isotropic case when $t^2 = r^2 = 1/2$, this critical point is called the *isotropic CC critical point*. In the generic anisotropic case when $t^2 = 1 - r^2 \neq 1/2$, this critical point is called the *anisotropic CC critical point*.

5. Phase diagram without dimerization

All four boundaries of parameter space (2.8) shown as the sides of the square in Fig. 12(a) evade localization. Three of these boundaries belong to the unitary class, one to the symplectic class. Any deviation away from these boundaries puts the two-dimensional spin-directed \mathbb{Z}_2 network model in the two-dimensional symplectic class of Anderson localization. The symplectic class for disordered metals is the most robust to the effects of disorder in that it displays the phenomenon of weak antilocalization for any dimensionality, i.e., the perturbative effect of

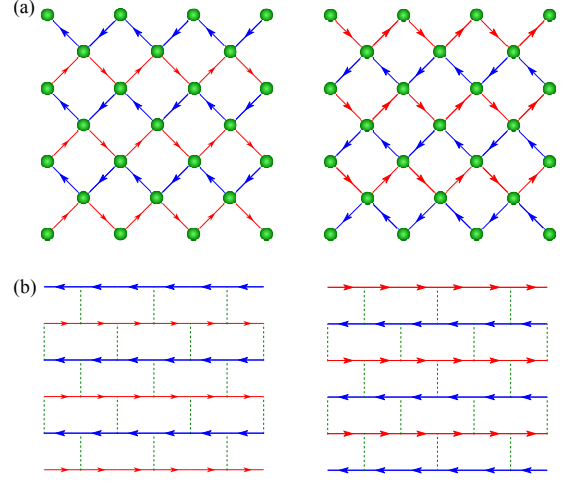


FIG. 11. (Color online:) When $\delta^2 = \theta - \pi/2 = 0$, the two-dimensional spin-directed \mathbb{Z}_2 network model from Fig. 6 decouples into two directed CC network models that are related by time reversal. Panels (a) and (b) are drawn using the vertex and the brick-wall representations, respectively. Since all elementary scattering 2×2 blocks in Eq. (2.20) are the same, criticality holds for any $0 \leq t^2 \leq 1$. At the isotropic point $t^2 = r^2 = 1/2$, the system exhibits the criticality of the usual isotropic CC model, otherwise the system exhibits the critical behavior of the anisotropic CC model.

disorder in the diffusive metallic regime is to enhance the conductivity in the symplectic class.⁵¹ Hence, the most economical conjecture regarding the nature of the interior of parameter space (2.8) with regard to the physics of localization is that it is metallic. This scenario is confirmed by our numerical calculations that we present in Sec. III except for the region where $t^2 \ll 1$. Although the numerical results in this region are inconclusive, we argue in favor of a metallic phase. In fact, the effective Dirac Hamiltonian derived for $t^2 \ll 1$ in Appendix A is nothing but the Hamiltonian studied by Mong *et al.*³⁶ with additional anisotropy in velocities. Their numerical results imply that this region of question is metallic. We can thus conclude that there is only a metallic phase in the interior of the square in Fig. 12(a).

6. Phase diagram with dimerization

We close Sec. II with the summary of our numerical results, to be described in more detail in Sec. III, in the form of the cuts of the schematic three-dimensional phase diagram displayed in Fig. 12(c).

Any non-vanishing dimerization δ^2 shrinks parameter space (2.8) through the condition

$$\delta^2 \leq t^2 \leq 1 - \delta^2. \quad (2.21)$$

According to Appendix B, the continuum limit of the two-dimensional spin-directed \mathbb{Z}_2 network model in the vicinity of $\theta = 0$ is that of a gapless Hamiltonian for

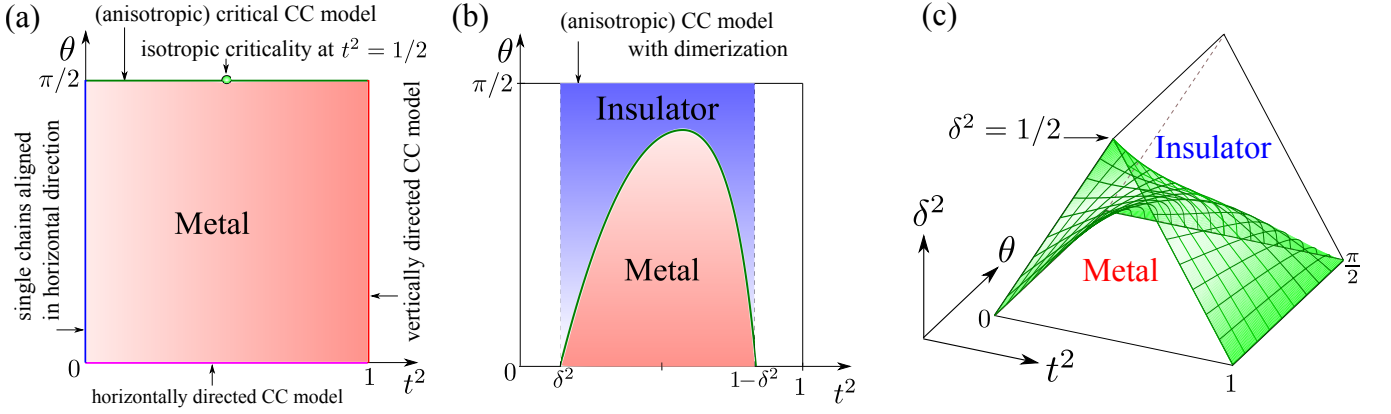


FIG. 12. (Color online:) (a) Phase diagram in the two-dimensional parameter space (a square) (2.8) without dimerization of the two-dimensional spin-directed \mathbb{Z}_2 network model. The boundaries of the square corresponds to a two-dimensional chiral metal when $\theta = 0$, a two-dimensional chiral metal when $t = 1$, the metal-insulator critical point of the (two-dimensional) CC model when $\theta = \pi/2$, and the quasi-one-dimensional symplectic metallic fixed point when $t^2 = 0$. Numerics of the two-dimensional spin-directed \mathbb{Z}_2 network model are consistent with a metallic phase in the interior of the square except in the region of $t^2 \ll 1$ for which numerics are inconclusive. However, we show in Appendix A that the numerical results from Ref. 36 apply to this region, thereby implying that this region is metallic. (b) Two-dimensional cut of the phase diagram in the three-dimensional parameter space (2.7) with *fixed and non-vanishing* dimerization of the two-dimensional spin-directed \mathbb{Z}_2 network model. The presence of the dimerization improves the quality of the numerics. Dimerization reduces the area of the metallic phase. The divergences of the localization length at the metal-insulator transitions are consistent with a metal-insulator critical point belonging to the two-dimensional symplectic class of Anderson localization. (c) Qualitative phase diagram in the three-dimensional parameter space (2.7) with *fixed and non-vanishing* dimerization. The phase diagram that includes the effect of the sign of the dimerization in Eq. (2.7) can be represented by gluing along the negative δ^2 axis the mirror image about the plane $\delta^2 = 0$ of the phase diagram for positive δ^2 . This delivers two insulating phases separated by a metallic phase.

any allowed value of t^2 and δ^2 in the three-dimensional parameter space (2.7). Hence, we anticipate a metallic phase when $\theta = 0$ in the three-dimensional parameter space (2.7). According to Appendix B, the continuum limit of the two-dimensional spin-directed \mathbb{Z}_2 network model in the vicinity of $\theta = \pi/2$ is that of a massive Dirac equation for any allowed value of t^2 and $\delta^2 \neq 0$ in the three-dimensional parameter space (2.7). Hence, we anticipate an insulating phase when $\theta = \pi/2$ and $\delta^2 \neq 0$ in the three-dimensional parameter space (2.7). Incidentally, a numerical study of two-component Dirac fermions with random mass and random potentials from Ref. 52 supports this conclusion. On the boundary $t^2 = \delta^2$ or $1 - \delta^2$ of the three-dimensional parameter space (2.7),

propagation is unidirectional. This boundary, if supplemented by the condition $\theta = 0$, is the end line of a critical surface at which a metal-insulator transition takes place in the three-dimensional parameter space (2.7). On the insulating side of this quantum phase transition, dimerization is strong relative to the disorder strength in that the density of states is so low in the presence of disorder that localization rules. On the metallic side of this quantum phase transition, dimerization is weak relative to the disorder strength in that the metallic fixed point in the two-dimensional symplectic symmetry class of Anderson localization is realized. From these considerations, we conjecture the schematic three-dimensional phase diagram shown in Fig. 12(c). We now present numerical support for the phase diagram 12(c).

III. NUMERICAL DATA WITH DIMERIZATION

A. Transfer matrix

In numerical studies of network models, it is convenient to do a similarity transformation on the space of scattering states. Instead of defining a two-dimensional spin-directed \mathbb{Z}_2 network model by a unitary scattering matrix that maps $2M$ incoming plane waves into $2M$ outgoing plane waves, we can do a similarity transformation on the scattering states under which a unitary scattering matrix turns into a pseudo-unitary transfer matrix. The transfer matrix maps the plane waves at the bottom of the brick wall to the plane waves at the top of the brick wall if the boundary conditions are those of Fig. 13(a). If the boundary conditions are those of Fig. 13(b), the transfer matrix maps the

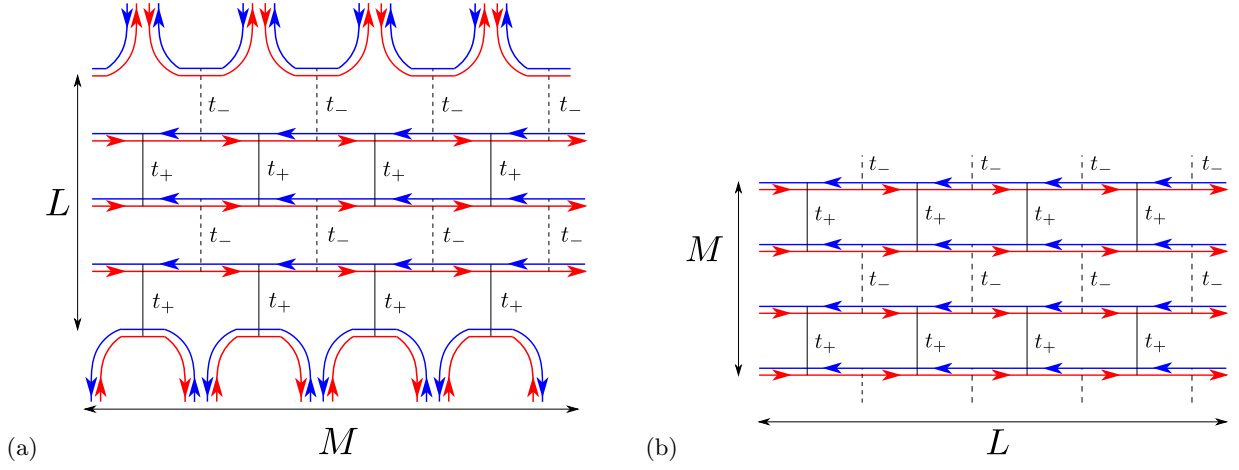


FIG. 13. (Color online:) Two examples in the brick-wall representation of two-dimensional spin-directed \mathbb{Z}_2 network models built out of the elementary scattering processes shown in Fig. 5. The periodic choice of the transmission amplitudes t_+ and t_- implements a dimerization pattern. The red and blue lines represent the flow of electron with up and down spins, respectively. The continuous (dotted) black line represents the scattering with transmission amplitude t_+ (t_-) between them. Periodic boundary conditions are imposed along the horizontal and vertical directions in panels (a) and (b), respectively. The geometrical dimensions of these two-dimensional spin-directed \mathbb{Z}_2 network models are $M \times L = 8 \times 4$ and $L \times M = 8 \times 4$ for examples (a) and (b), respectively.

plane waves at the left of the brick wall to the plane waves at the right of the brick wall. In the former case, the elementary transfer matrix is defined by

$$\begin{pmatrix} \psi_{2,\uparrow}^{(i)} \\ \psi_{1,\downarrow}^{(i)} \\ \psi_{1,\uparrow}^{(o)} \\ \psi_{2,\downarrow}^{(o)} \end{pmatrix} = \mathcal{M}_\perp \begin{pmatrix} \psi_{4,\uparrow}^{(i)} \\ \psi_{3,\downarrow}^{(i)} \\ \psi_{3,\uparrow}^{(o)} \\ \psi_{4,\downarrow}^{(o)} \end{pmatrix}, \quad \mathcal{M}_\perp := \begin{pmatrix} +\frac{r}{t} e^{-i\phi_3} Q & -\frac{1}{t} e^{-i\phi_0} Q \\ +\frac{1}{t} e^{+i\phi_0} Q & -\frac{r}{t} e^{+i\phi_3} Q \end{pmatrix}. \quad (3.1a)$$

In the latter case, the elementary transfer matrix is defined by

$$\begin{pmatrix} \psi_{1,\uparrow}^{(o)} \\ \psi_{3,\uparrow}^{(o)} \\ \psi_{1,\downarrow}^{(i)} \\ \psi_{3,\downarrow}^{(i)} \end{pmatrix} = \mathcal{M}_\parallel \begin{pmatrix} \psi_{2,\uparrow}^{(i)} \\ \psi_{4,\uparrow}^{(i)} \\ \psi_{2,\downarrow}^{(o)} \\ \psi_{4,\downarrow}^{(o)} \end{pmatrix}, \quad (3.2a)$$

where

$$\mathcal{M}_\parallel := \frac{1}{r^2 + t^2 \cos^2 \theta} \begin{pmatrix} r e^{+i(\phi_0 + \phi_3)} & t e^{+i(\phi_0 + \phi_1)} \cos \theta & -t^2 e^{+i(\phi_1 + \phi_2)} \sin \theta \cos \theta & r t e^{+i(\phi_2 + \phi_3)} \sin \theta \\ -t e^{+i(\phi_0 - \phi_1)} \cos \theta & r e^{+i(\phi_0 - \phi_3)} & -r t e^{+i(\phi_2 - \phi_3)} \sin \theta & -t^2 e^{-i(\phi_1 - \phi_2)} \sin \theta \cos \theta \\ t^2 e^{-i(\phi_1 + \phi_2)} \sin \theta \cos \theta & -r t e^{-i(\phi_2 + \phi_3)} \sin \theta & r e^{-i(\phi_0 + \phi_3)} & t e^{-i(\phi_0 + \phi_1)} \cos \theta \\ r t e^{-i(\phi_2 - \phi_3)} \sin \theta & t^2 e^{+i(\phi_1 - \phi_2)} \sin \theta \cos \theta & -t e^{-i(\phi_0 - \phi_1)} \cos \theta & r e^{-i(\phi_0 - \phi_3)} \end{pmatrix}. \quad (3.2b)$$

We refer the reader to Ref. 42 for the detailed construction of the total transfer matrix \mathcal{M}_{tot} corresponding to Fig. 13 from the elementary 4×4 transfer matrix of Eq. (3.2).

B. Definition of the normalized localization length

As explained in Ref. 42, the transfer matrix \mathcal{M}_{tot} is pseudo-unitary and belongs to the group $SO^*(2M)$ given the definition of M in Fig. 13 (M is even). The matrix $\mathcal{M}_{\text{tot}}^\dagger \mathcal{M}_{\text{tot}}$ is positive definite and has the dou-

bly degenerate eigenvalues of the form $\exp(\pm 2X_j)$ with $j = 1, \dots, M/2$, which can be ordered according to the convention

$$0 < X_1 < \dots < X_{M/2}. \quad (3.3)$$

The ordered numbers X_j with $j = 1, \dots, M/2$ are called Lyapunov exponents. They become selfaveraging random variables as the quasi-one-dimensional limit $L \rightarrow \infty$ for fixed M is taken in Fig. 13.⁵³ The quasi-one-dimensional localization length is defined by

$$\xi_M := \lim_{L \rightarrow \infty} \frac{L}{X_1}. \quad (3.4)$$

As shown by MacKinnon and Kramer,⁵⁴ criticality in two dimensions can be probed through the dependence of the normalized localization length

$$\Lambda := \frac{\xi_M}{M} \quad (3.5)$$

on the width M of the quasi-one-dimensional spin-directed network model in Fig. 13. We are going to study numerically the dependence on M of the normalized localization lengths Λ_\perp and Λ_\parallel defined by the geometries of Fig. 13(a) and 13(b), respectively. To this end, we shall use the transfer matrix method from Ref. 54 in a quasi-one-dimensional geometry with the aspect ratio $L/M = 5 \times 10^5$. We work in the parameter space (2.7).

C. Finite-size scaling for the normalized localization length in the presence of dimerization

To begin with, we choose the one-dimensional cut

$$(0.5, \pi/4, \delta^2), \quad \delta^2 \in [0, 0.5], \quad (3.6)$$

of three-dimensional parameter space (2.7). This cut is far from the isotropic CC critical point

$$(0.5, \pi/2, 0). \quad (3.7)$$

Figures 14(a-1) and 14(b-1) show the δ^2 dependence of the normalized localization lengths Λ_\perp and Λ_\parallel defined by the geometries of Fig. 13(a) and 13(b), respectively, along the cut (3.6) as the width M is increased from $M = 16$ to $M = 320$. According to Fig. 14(a-1), Λ_\perp and Λ_\parallel increase (decrease) with increasing M for small (large) values of δ^2 . The dependence on M of either Λ_\perp or Λ_\parallel appears to vanish at a value of δ^2 approximately given by 0.23. This suggests that the point

$$(t_c^2, \theta_c, \delta_c^2) := (0.5, \pi/4, 0.23) \quad (3.8)$$

in the three-dimensional parameter space (2.7) is a critical point at which a metal-insulator transition takes place.

To confirm this interpretation of the point (3.8) in the three-dimensional parameter space (2.7), we have done a finite-size scaling analysis of the data presented in Fig. 14(a-1) and 14(b-1), the details of which are to be found in Ref. 55.

Figures 14(a-2) and 14(b-2) support the one-parameter scaling obeyed by Λ'_\perp and Λ'_\parallel . Here, Λ'_\perp and Λ'_\parallel denote the action of subtracting from Λ_\perp and Λ_\parallel , respectively, corrections to their M dependences that are caused by the leading irrelevant perturbations to the critical point (3.8) in the three-dimensional parameter space (2.7).

The first two lines of Table I give, at the critical point (3.8) along the cut (3.6), the value of the critical exponent ν that controls the power-law divergence of the localization length, the value $|y|$ for the leading irrelevant scaling exponent y , the strength of δ_c^2 , the values of the normalized localization length Λ_\perp^c and Λ_\parallel^c , and their geometrical mean $\sqrt{\Lambda_\perp^c \Lambda_\parallel^c}$.

The subsequent two pairs of lines from Table I summarize the results of the same analysis performed along the one-dimensional cuts

$$(0.5, 5\pi/16, \delta^2), \quad \delta^2 \in [0, 0.5], \quad (3.9)$$

and

$$(0.6, \pi/4, \delta^2), \quad \delta^2 \in [0, 0.4], \quad (3.10)$$

in the three-dimensional parameter space (2.7) (see Ref. 55).

The value for the critical point δ_c along a one-dimensional cut with t and θ fixed in the three-dimensional parameter space (2.7) obtained from Λ_\perp agrees within error bars with that obtained from Λ_\parallel . This agreement is required if (t, θ, δ_c) is to be interpreted as a quantum critical point in Anderson localization.

We find the values of the scaling exponent ν to be distributed around 2.7 ± 0.2 in Table I. For comparison, the scaling exponent ν for the ordinary two-dimensional symplectic class is $\nu \approx 2.7$.⁵⁶

In contrast, we observe that the normalized localization lengths at the critical point Λ_\perp^c and Λ_\parallel^c along a given one-dimensional cut in the three-dimensional parameter space (2.7) from Table I differ. These values also differ along different cuts in the three-dimensional parameter space (2.7) as well as from the value $\Lambda^c \approx 1.84$ obtained for the ordinary two-dimensional symplectic class in Ref. 56. However, if we take the geometric average of Λ_\perp^c and Λ_\parallel^c , we find that the value

$$\sqrt{\Lambda_\perp^c \Lambda_\parallel^c} \approx 1.84 \quad (3.11)$$

agrees with Λ^c . The result that the geometric average of Λ_\perp^c and Λ_\parallel^c for the two-dimensional spin-directed \mathbb{Z}_2 network model agrees with the value Λ^c for the two-dimensional \mathbb{Z}_2 network model from Ref. 42 has a counterpart for the CC network model. In the anisotropic CC network model defined by the condition $0 \leq t^2 \neq 1/2 \leq 1$, there are two normalized localization lengths Λ_\perp^c and Λ_\parallel^c whose geometric average equals the normalized localization length of the isotropic CC network model defined

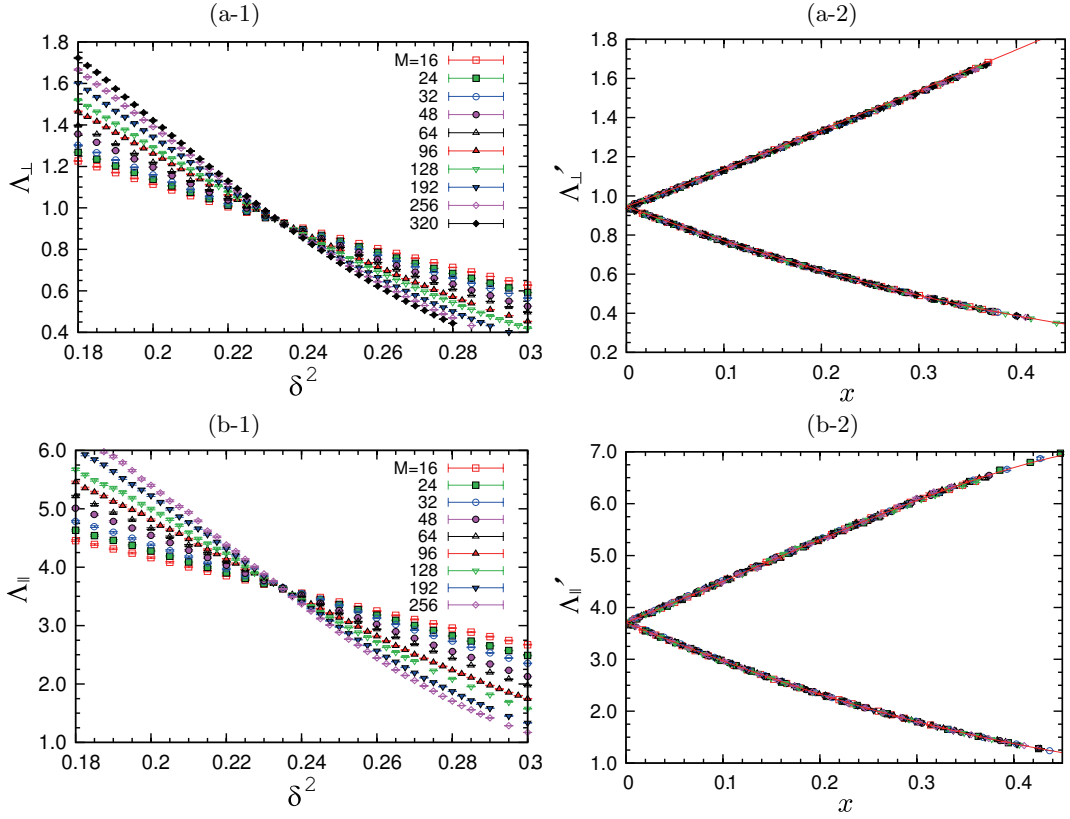


FIG. 14. (Color online:) The two-dimensional spin-directed \mathbb{Z}_2 network model is solved numerically along the one-dimensional cut (3.6) in the three-dimensional parameter space (2.7). Panel (a-1) shows the δ^2 dependence of the normalized localization length Λ_{\perp} corresponding to the geometry of Fig. 13(a) for several values of M . Panel (b-1) shows the δ^2 dependence of the normalized localization lengths Λ_{\parallel} corresponding to the geometry of Fig. 13(b) for several values of M . A finite-size scaling analysis of panels (a-1) and (b-1) is performed in panels (a-2) and (b-2), respectively. The horizontal axis is $x = M^{1/\nu}|\delta^2 - \delta_c^2|$ with ν and δ_c^2 given in Table S-I and Table S-II from Ref. 55. The vertical axis Λ'_x with $x = \perp, \parallel$ is defined by subtracting from the normalized localization length Λ_x its finite-size correction from the leading irrelevant exponent y given in Table S-I and Table S-II from Ref. 55. The red solid curve demonstrates the quality of the data collapse onto a one-parameter scaling function.

by the condition $t^2 = 1/2$.⁵⁰ In either cases, this relation is a manifestation of two-dimensional conformal invariance at a critical point.⁵⁷

The difference between Λ_{\perp}^c and Λ_{\parallel}^c along the cut (3.9) is smaller than that along the cut (3.6). This observation is consistent with the fact that the former cut is closer than the latter cut to the isotropic CC critical point (3.7).

The difference between Λ_{\perp}^c and Λ_{\parallel}^c along the cut (3.10) is smaller than that along the cut (3.6). We attribute this fact to the property that increasing small t increases Λ_{\perp} , while it decreases Λ_{\parallel} .

From these observations, we conjecture that the surface states of weak three-dimensional \mathbb{Z}_2 topological insulators undergo a metal-insulator transition as a result of the competition between disorder and dimerization that belongs to the ordinarily two-dimensional symplectic universality class.

D. Finite-size scaling for the normalized localization length in the absence of dimerization

We assume no dimerization, i.e., $\delta^2 = 0$ and fix, without loss of generality, θ to the value $\pi/4$. The size dependence of the normalized localization length Λ_{\perp} and Λ_{\parallel} corresponding to the geometries of Figs. 13(a) and 13(b), respectively, as t^2 is increased along the interval $[0, 1]$ is the following.

Figure 15 shows the normalized localization length Λ_{\perp} in panel (a) and Λ_{\parallel} in panel (b) as a function of t^2 .

On the one hand, according to Fig. 15(b), Λ_{\parallel} increases with increasing M for values of t^2 ranging from 0.05 to 0.95. This would be the signature for a metallic phase for these values of t^2 if we could show that Λ_{\perp} also diverges in the limit $M \rightarrow \infty$. According to Fig. 15(a), Λ_{\perp} also increases with increasing M for t^2 larger than 0.05. We conclude that the phase at $\delta^2 = 0$, $\theta = \pi/4$, and for $0.05 < t^2 < 0.95$ is metallic.

For values of t^2 smaller than 0.05, Λ_{\perp} decreases with

TABLE I. Summary of the finite-size scaling analysis for $\Gamma_x (= 1/\Lambda_x)$ with $x = \perp, \parallel$ for the three cuts (3.6), (3.9), and (3.10) from the three-dimensional parameter space (2.7). Only the most important fitting parameters, namely ν , y , δ_c^2 , Λ_x^c , and $\sqrt{\Lambda_\perp^c \Lambda_\parallel^c}$ are shown. More details on this finite-size scaling analysis can be found in Ref. 55. The expected value and its error bar are estimated by employing the practical error bar procedure.⁵⁸

x	θ	t^2	ν	$ y $	δ_c^2	Λ_x^c	$\sqrt{\Lambda_\perp^c \Lambda_\parallel^c}$
\perp	$\pi/4$	0.5	2.89 [2.75 : 2.98]	0.72 [0.59 : 0.90]	0.2340 [0.2334 : 0.2349]	0.935 [0.919 : 0.944]	1.849
\parallel	$\pi/4$	0.5	2.71 [2.53 : 2.85]	0.47 [0.30 : 0.81]	0.2343 [0.2332 : 0.2355]	3.657 [3.557 : 3.734]	
\perp	$5\pi/16$	0.5	2.80 [2.64 : 2.91]	0.91 [0.55 : 1.49]	0.1591 [0.1579 : 0.1616]	1.290 [1.234 : 1.310]	1.850
\parallel	$5\pi/16$	0.5	2.63 [2.55 : 2.79]	1.14 [0.55 : 1.54]	0.1590 [0.1575 : 0.1598]	2.652 [2.622 : 2.716]	
\perp	$\pi/4$	0.6	2.84 [2.70 : 2.92]	0.81 [0.51 : 1.21]	0.2765 [0.2752 : 0.2784]	1.225 [1.193 : 1.249]	1.834
\parallel	$\pi/4$	0.6	2.57 [2.42 : 2.74]	0.85 [0.26 : 1.72]	0.2764 [0.2754 : 0.2772]	2.746 [2.710 : 2.783]	

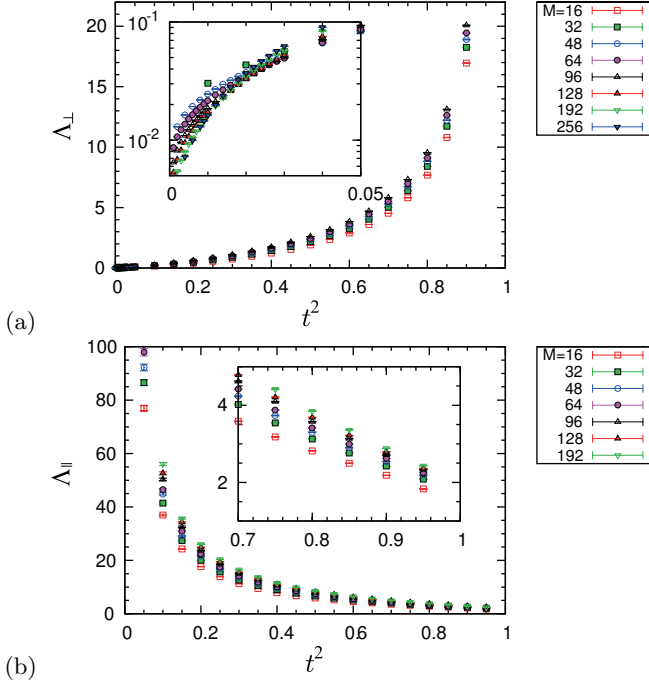


FIG. 15. (Color online:) The t^2 dependence of the normalized localization lengths Λ_\perp in panel (a) and Λ_\parallel in panel (b) of the two-dimensional spin-directed \mathbb{Z}_2 network model without dimerization, at $\theta = \pi/4$, and for fixed M ranging from 16 to 256. Inset: Dependence on t^2 near $t^2 = 0$ for panel (a) and near $t^2 = 1$ for panel (b).

increasing M very close to $t^2 = 0$ according to the inset of Fig. 15(a). However, this apparent insulating dependence on M of Λ_\perp for $t^2 < 0.05$ might be a finite-size artifact due to the fact that Λ_\perp must vanish at $t^2 = 0$. In this scenario, the value of M beyond which metallic dependence of Λ_\perp on M is the rule diverges as $t^2 \rightarrow 0$. This scenario is consistent with the observation that the goodness of fit (see its definition in Ref. 55) is the poorest for $t^2 < 0.05$. Moreover, the following argument supports this scenario and the conclusion that the phase is metallic inside the two-dimensional cut of parameter space at $\delta^2 = 0$.

When $t^2 = 0$, the two-dimensional spin-directed \mathbb{Z}_2 network model realizes a unidirectional metal that consists of M (even) independent pairs of helical edge states supporting the dimensionless conductance M along their direction of propagation [the direction \parallel in the geometry of Fig. 15(b)] and a vanishing conductance in the orthogonal direction [the direction \perp in the geometry of Fig. 15(a)]. We first assume that $\lim_{M \rightarrow \infty} \Lambda_\perp = 0$, where the limit $M \rightarrow \infty$ is taken with M even, persists away from $t^2 = 0$ for sufficiently small values of t^2 . We are going to show that this first assumption contradicts the second assumption $\lim_{M \rightarrow \infty} \Lambda_\parallel = \infty$, where the limit $M \rightarrow \infty$ is taken with M even, for all values of t^2 . [The second assumption is supported empirically for all the values of t^2 shown in Fig. 15(b), whereas the first assumption is not unambiguously supported by Fig. 15(a).] These two assumptions are in mutual contradiction, for the first assumption implies that the two-dimensional spin-directed \mathbb{Z}_2 network model realizes a quasi-one-dimensional quantum wire with an even number $2M$ of channels in the symplectic symmetry class. Such a quasi-one-dimensional wire is necessarily localized, i.e., $\lim_{M \rightarrow \infty} \Lambda_\parallel = 0$, in contradiction with the second assumption. Since our finite-size scaling analysis puts the second assumption on firmer ground than the first assumption, we conclude that a two-dimensional metallic phase in the symplectic symmetry class is established for any non-vanishing t^2 .

IV. NUMERICAL DATA WITH TRIMERIZATION

As was emphasized in Refs. 40, 59, and 60, weak three-dimensional \mathbb{Z}_2 topological insulators are characterized by a dependence on the parity in the stacking number of strong two-dimensional \mathbb{Z}_2 topological insulators. This parity effect can be illustrated in the context of the two-dimensional spin-directed \mathbb{Z}_2 network model by weakly perturbing the quasi-one-dimensional symplectic metallic fixed point (2.9) from Sec. II C 1 in the limit M fixed and $L \rightarrow \infty$. In this quasi-one-dimensional limit,

the localization properties of the two-dimensional spin-directed \mathbb{Z}_2 network model depend on the parity of M . If $M = 2M'$ is even, as we have assumed all along so far, then the transfer matrix belongs to the Lie group $SO^*(4M')$ and exponential localization is the rule.⁶¹ If $M = 2M' + 1$ is odd, the transfer matrix belongs to the Lie group $SO^*(4M' + 2)$ and there is one pair of Kramers degenerate helical states that is perfectly conducting.⁶⁻⁸ Correspondingly, if we stack and weakly couple an odd number of strong two-dimensional \mathbb{Z}_2 topological insulators, we expect delocalization of at least one surface state.

The following parity effect follows from the parity effect discussed above if we assume $t_+ \gg t_-$ in Fig. 16. In this limit, we may replace the three pairs of helical modes in a trimer by a single effective pair of helical modes, which is then coupled by t_- to its neighboring effective pairs of helical modes. Thus, the two-dimensional trimerized spin-directed \mathbb{Z}_2 network model reduces to a two-dimensional spin-directed \mathbb{Z}_2 network model without polymerization in this limit. In the opposite limit $t_+ \ll t_-$, any two pairs of helical modes coupled by t_- become inert (localized) and the remaining pairs of helical modes are weakly coupled without polymerization. The same conclusion follows from the point of view of surface states realizing an even number of Dirac cones. Scattering matrix elements are needed that couple pairwise the surface Dirac cones in order to localize the Dirac modes. Trimerization does not deliver such matrix elements.

From the examples of dimerization and trimerization, we conjecture the following parity effect. The combined effects of polymerization and disorder for the two-dimensional spin-directed \mathbb{Z}_2 network model produces a phase diagram with either (i) two insulating phases separated by a metallic phase when the breaking of translation symmetry involves a repeat unit cell consisting of an even number of helical modes in the clean limit, (ii) or a single metallic phase when the breaking of translation symmetry involves a repeat unit cell consisting of an odd number of helical modes in the clean limit.

A. Transfer matrix

Two transfer matrices \mathcal{M}_\perp and \mathcal{M}_\parallel are defined as in Sec. III A, except for the pattern of trimerization shown in Fig. 16 for the transmission amplitude.

B. Definition of the normalized localization length

The normalized localization lengths Λ_\perp and Λ_\parallel are defined as in Sec. III B, except for the pattern of trimerization shown in Fig. 16 for the transmission amplitude.

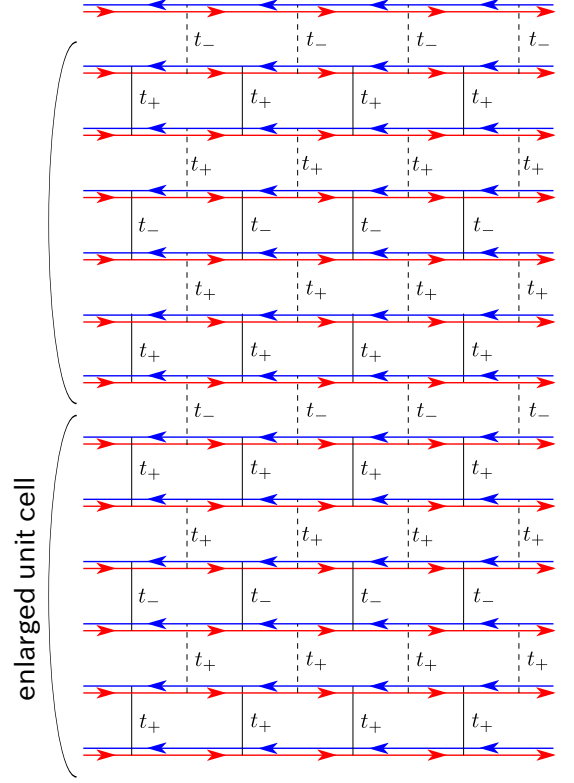


FIG. 16. (Color online:) Two-dimensional spin-directed \mathbb{Z}_2 network model with $M = 6M'$ an even integer multiple of 3. The periodic pattern for the transmission amplitudes implements a trimerization, as is indicated by the enlarged unit cell.

C. Finite-size scaling for the normalized localization length in the presence of trimerization

Figure 17 shows the δ^2 dependence of the normalized localization lengths Λ_\perp and Λ_\parallel with $t_\pm^2 = 0.5 \pm \delta^2$ and $\theta = \pi/4$ in the two-dimensional trimerized spin-directed \mathbb{Z}_2 network model.

According to Fig. 17(a), the normalized localization length Λ_\perp at fixed $t_\pm^2 = 0.5 \pm \delta^2$, $\theta = \pi/4$, and δ^2 increases with increasing M , whereas it is a decreasing function with increasing δ^2 at fixed $t_\pm^2 = 0.5 \pm \delta^2$, $\theta = \pi/4$, and M . The latter decrease of Λ_\perp with increasing δ^2 is expected since $t_-^2 = 0$ at $\delta^2 = 0.5$.

According to Fig. 17(b), the normalized localization length Λ_\parallel at fixed $t_\pm^2 = 0.5 \pm \delta^2$, $\theta = \pi/4$, and δ^2 increases with increasing M . Moreover, it is an increasing function of δ^2 at fixed $t_\pm^2 = 0.5 \pm \delta^2$, $\theta = \pi/4$, and M .

Thus, there is no sign of a transition from a metallic to an insulating phase in the two-dimensional trimerized spin-directed \mathbb{Z}_2 network model upon increasing the value of δ^2 , as was the case for the two-dimensional dimerized spin-directed \mathbb{Z}_2 network model at the critical point (3.8), see Fig. 14.

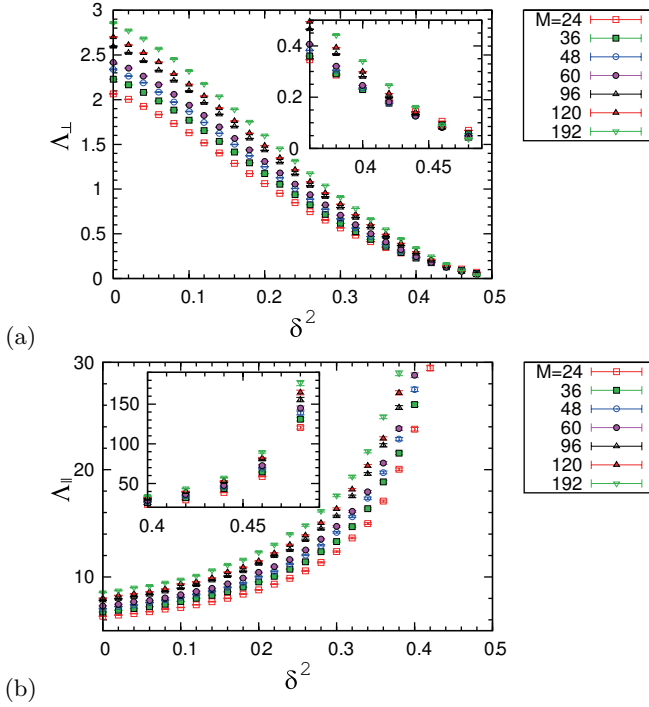


FIG. 17. (Color online:) Combined effects of trimerization and disorder for a two-dimensional spin-directed \mathbb{Z}_2 network model. The δ^2 dependence of the normalized localization length at $t^2 = 0.5$ and $\theta = \pi/4$ for fixed M ranging from 24 to 192 is shown in panel (a) for Λ_{\perp} and in panel (b) for Λ_{\parallel} . Inset: Dependence on δ^2 near $\delta^2 = 0.5$ for panel (a) and for panel (b).

V. SUMMARY AND DISCUSSION

We have shown that the surface states of a weak three-dimensional \mathbb{Z}_2 topological insulator can be modeled by a two-dimensional spin-directed \mathbb{Z}_2 network model. In other words, a two-dimensional spin-directed \mathbb{Z}_2 network model can be interpreted as an effective lattice regularization for the surface states of a weak three-dimensional \mathbb{Z}_2 topological insulator. The qualifier \mathbb{Z}_2 indicates here that time-reversal symmetry is present, but $SU(2)$ spin-rotation symmetry is broken.

We have studied the combined effects of polymerization and disorder in a two-dimensional spin-directed \mathbb{Z}_2 network model. Polymerization implies that the lattice symmetry group \mathfrak{G} of the two-dimensional spin-directed \mathbb{Z}_2 network model is reduced to a nontrivial subgroup \mathfrak{G}' in the clean limit.

On the one hand, if the polymerization opens a spectral gap in the clean limit and if the disorder strength is weak relative to the polymerization gap, single-particle states are localized. As the ratio of the disorder strength to the polymerization gap is increased, a quantum phase transition from an insulating to a metallic phase takes place. This transition is smooth and we have shown that it belongs to the two-dimensional symplectic universality class in the theory of Anderson localization, as measured

by the power-law divergence of the localization length with the scaling exponent $\nu \approx 2.7$. This metallic phase is connected to the critical point that separates the two polymerized-gapped phases in the clean limit.

On the other hand, if the polymerization does not open a spectral gap in the clean limit, i.e., if the pattern of symmetry breaking $\mathfrak{G} \rightarrow \mathfrak{G}'$ is associated to an enlarged unit cell of the two-dimensional spin-directed \mathbb{Z}_2 network model that is built out of an odd integer number of the unit cell prior to switching on polymerization, then the metallic phase is robust to any short-range correlated disorder.

The two-dimensional spin-directed \mathbb{Z}_2 network model studied in this paper is the second example of a two-dimensional directed network model after that of the directed CC network model. Similarly to the directed CC network model, it is an effective lattice model that captures some low-energy and long-wave length properties of surface states of weak three-dimensional topological insulators, such as the universal properties of a quantum phase transition from the theory of Anderson localization. There is an important difference with regard to the long-distance physics of the two classes of network models, however. Charge transport for the directed CC network model is intrinsically anisotropic: ballistic chiral transport in one direction and critical (diffusive) transport in the other direction. By contrast, charge transport for the spin-directed \mathbb{Z}_2 network model is effectively isotropic at long wave lengths, as is illustrated after a rescaling of velocities in the limiting Dirac Hamiltonians.

There exists a network model for each of the ten symmetry classes in the theory of Anderson localization.⁶² Regardless of the dimensionality of space, five of these network models encode the effects of disorder on strong topological insulators, noninteracting insulators with response functions whose topological character are protected by symmetry.^{63–65} By stacking and weakly coupling a family of strong two-dimensional topological insulators from a given symmetry class, one obtains a weak three-dimensional topological insulator. We conjecture that the combined effects of breaking the stacking symmetry in a periodic way (polymerization) and disorder on the phase diagram of a weak three-dimensional topological insulator from a given symmetry class are captured by a two-dimensional “directed” network model built out of an elementary scattering matrix within this symmetry class. As we have seen for the two-dimensional spin-directed \mathbb{Z}_2 network model of this paper, and as expected from theoretical considerations,^{38,52,66–68} unpolymerized network models are not expected to support insulating phases. Furthermore, the dichotomy between anisotropic versus isotropic transport is expected to apply to the three symmetry classes with a \mathbb{Z} index (the symmetry classes A, C, and D) and the two symmetry classes with a \mathbb{Z}_2 index (the symmetry classes AII and CII), respectively.³⁸

An outstanding open problem is the interplay of disorder and interactions for the surface states of three-

dimensional weak \mathbb{Z}_2 topological insulators, given the fact that interactions can stabilize states of matter that fall outside the classification of noninteracting topological insulators.^{66,69–81}

ACKNOWLEDGMENTS

We thank Jens Bardarson for helpful discussions. S. R., A. F., and C. M. thank the KITP program Topological Insulators and Superconductors for hospitality where this work was initiated. H. O. was supported by Grant-in-Aid (Nos. 25800213 and 25390113) from the Japan Society for Promotion of Science. The work of A. F. was partly supported by a Grant-in-Aid (No. 24540338) from the Japan Society for Promotion of Science and by the RIKEN iTHES project.

Appendix A: Quasi-one-dimensional model for the surface states of a weak three-dimensional \mathbb{Z}_2 topological insulator

1. Definition

Figure 1 depicts a two-dimensional \mathbb{Z}_2 topological *band* insulator. The interior of the ellipse shown in Fig. 1(a) is called the bulk. The boundary of the ellipse shown in Fig. 1(a) is the edge. Figure 1 represents a model of noninteracting electrons such that (i) the single-particle eigenstates with support in the bulk display a spectral gap Δ as is indicated in Fig. 1(b), while (ii) the single-particle eigenstates with support on the edge realize a two-fold degenerate dispersion that crosses the spectral gap of the bulk states as is indicated in Fig. 1(b), are extended along the edge, but are exponentially localized in the direction perpendicular to the edge. These edge states represent a single pair of Kramers' degenerate electrons propagating with opposite velocities. These edge states are also called helical states as the expectation values of the electronic spins are opposite for each electron forming the Kramers' degenerate pair and change with the momenta k of the electrons parallel to the edge. The low-energy and long-wave-length effective Hamiltonian of the single pair of helical states depicted in Fig. 1(a) is

$$\hat{H}_{\text{Helical}} := \int_{\text{edge}} dx \left(\hat{\Psi}^\dagger(-i) v \sigma_3 \partial_x \hat{\Psi} \right) (x). \quad (\text{A1a})$$

Units are chosen so that $\hbar = 1$. The speed v is positive by convention. The operators $\hat{\Psi}_\alpha^\dagger(x)$ and $\hat{\Psi}_\alpha(x)$ create and destroy at the position x along the edge an electron with the projection $\alpha = \uparrow, \downarrow$ of its spin along the spin quantization axis, respectively. They make up the doublet of operators $\hat{\Psi}^\dagger(x)$ and $\hat{\Psi}(x)$, respectively. The Pauli matrices σ_1, σ_2 , and σ_3 act on the spin components of the electrons. The unit 2×2 matrix in spin space is denoted σ_0 . Hamiltonian (A1a) is invariant under the operation of time reversal defined by

$$\hat{\Psi}^\dagger(x) = \hat{\Psi}'^\dagger(x) K \sigma_2, \quad \hat{\Psi}(x) = \sigma_2 K \hat{\Psi}'(x), \quad (\text{A1b})$$

where K denotes the operation of complex conjugation.

A layered microscopic model that captures the tunneling of helical edge states between adjacent layers for energy scales below the bulk gap Δ is defined by the Hamiltonian

$$\begin{aligned} \hat{H}_{\text{layered}} := & \int_{\text{edge}} dx \sum_{n=1}^{2N} \left[\left(\hat{\Psi}_n^\dagger(-i) v_n \sigma_3 \partial_x \hat{\Psi}_n \right) (x) + \hat{\Psi}_n^\dagger(x) \mu_n(x) \sigma_0 \hat{\Psi}_n(x) \right] \\ & + \int_{\text{edge}} dx \sum_{n=1}^{2N-1} \left[\hat{\Psi}_{n+1}^\dagger(x) \left(\frac{\lambda_{n,0}}{2} \sigma_0 + i \sum_{j=1}^3 \frac{\lambda_{n,j}}{2} \sigma_j \right) \hat{\Psi}_n(x) + \text{H.c.} \right]. \end{aligned} \quad (\text{A2a})$$

There is an even number of layers $2N$. Each layer n with $n = 1, \dots, 2N$ has its own Fermi velocity $v_n > 0$ and chemical potential $\mu_n \in \mathbb{R}$. Any two consecutive layers are coupled by hopping matrix elements parametrized by the four independent real-valued couplings $\lambda_{\mu,n}$ with $\mu = 0, 1, 2, 3$ and $n = 1, \dots, 2N - 1$. Open boundary conditions are chosen along the layering axis. Hamiltonian (A2a) is invariant under the operation of time reversal defined by

$$\hat{\Psi}_n^\dagger(x) = \hat{\Psi}_n'^\dagger(x) K \sigma_2, \quad \hat{\Psi}_n(x) = \sigma_2 K \hat{\Psi}_n'(x), \quad (\text{A2b})$$

where K denotes the operation of complex conjugation and $n = 1, \dots, 2N$. Hamiltonian (A2a) is depicted in Fig. 2.

We can turn the layered model (A2) into a layered microscopic model of a weak three-dimensional \mathbb{Z}_2 topological *band* insulator by demanding that

$$v_n = v_{u,x} + (-1)^n v_s, \quad \mu_n = \mu_u + (-1)^n \mu_s, \quad \lambda_{n,\mu} = (1 - \delta_{n,2N}) [\lambda_{u,\mu} + (-1)^n \lambda_{s,\mu}], \quad \mu = 0, 1, 2, 3, \quad (\text{A3})$$

for $n = 1, \dots, 2N$. As we shall demonstrate, the continuum limit

$$\lim_{\substack{\lambda_{u,0} \rightarrow \infty \\ \mathbf{a}_y \rightarrow 0}} \frac{\lambda_{u,j}}{\lambda_{u,0}} = 0, \quad j = 1, 2, 3, \quad \lim_{\substack{\lambda_{u,0} \rightarrow \infty \\ \mathbf{a}_y \rightarrow 0}} \frac{\lambda_{s,\mu}}{\lambda_{u,0}} = 0, \quad \mu = 0, 1, 2, 3, \quad (\text{A4a})$$

where

$$\lim_{\substack{\lambda_{u,0} \rightarrow \infty \\ \mathbf{a}_y \rightarrow 0}} \frac{\lambda_{u,0}}{2} \times (2\mathbf{a}_y) \equiv v_{u,y} > 0 \quad (\text{A4b})$$

is a finite non-vanishing and positive number (\mathbf{a}_y is the interlayer lattice spacing), is related to Dirac fermions in a four-dimensional representation of the Clifford algebra in $(2+1)$ -dimensional space and time.

2. Generic stacked microscopic model and its continuum limit in the stacking direction

a. Definition

Motivated by Hamiltonian (A2a), we define Hamiltonian

$$\hat{H} := \int_{\text{edge}} dx \sum_{n=1}^{2N} \left\{ \hat{\Psi}_n^\dagger [\mathbf{V}_n (-i)\partial_x + \mathbf{U}_n] \hat{\Psi}_n + \left(\hat{\Psi}_n^\dagger \mathbf{T}_n \hat{\Psi}_{n+1} + \hat{\Psi}_{n+1}^\dagger \mathbf{T}_n^\dagger \hat{\Psi}_n \right) \right\}, \quad (\text{A5a})$$

whereby periodic boundary conditions have been assumed in the layering index n , i.e., $n + 2N \equiv n$, the 2×2 matrices \mathbf{V}_n and \mathbf{U}_n are Hermitean, and the 2×2 matrix \mathbf{T}_n is arbitrary. Reversal of time is implemented by the transformation

$$\hat{\Psi}_n^\dagger(x) = \hat{\Psi}_n'^\dagger(x) K \sigma_2, \quad \hat{\Psi}_n(x) = \sigma_2 K \hat{\Psi}_n'(x). \quad (\text{A5b})$$

If we write

$$\mathbf{V}_n = v_{n,0} \sigma_0 + v_{n,1} \sigma_1 + v_{n,2} \sigma_2 + v_{n,3} \sigma_3, \quad v_{n,\mu} \in \mathbb{R}, \quad \mu = 0, 1, 2, 3, \quad (\text{A6a})$$

$$\mathbf{U}_n = U_{n,0} \sigma_0 + U_{n,1} \sigma_1 + U_{n,2} \sigma_2 + U_{n,3} \sigma_3, \quad U_{n,\mu} \in \mathbb{R}, \quad \mu = 0, 1, 2, 3, \quad (\text{A6b})$$

and

$$\mathbf{T}_n = t'_{n,0} \sigma_0 + t'_{n,1} \sigma_1 + t'_{n,2} \sigma_2 + t'_{n,3} \sigma_3 + i (t''_{n,0} \sigma_0 + t''_{n,1} \sigma_1 + t''_{n,2} \sigma_2 + t''_{n,3} \sigma_3), \quad t'_{n,\mu}, t''_{n,\mu} \in \mathbb{R}, \quad \mu = 0, 1, 2, 3, \quad (\text{A6c})$$

we find that

$$\hat{H} = \hat{H}^{(e)} + \hat{H}^{(o)}. \quad (\text{A7a})$$

Here,

$$\begin{aligned} \hat{H}^{(e)} &= \int_{\text{edge}} dx \sum_{n=1}^{2N} \left\{ \hat{\Psi}_n^\dagger \left[\mathbf{V}_n^{(o)} (-i)\partial_x + \mathbf{U}_n^{(e)} \right] \hat{\Psi}_n + \left(\hat{\Psi}_n^\dagger \mathbf{T}_n^{(e)} \hat{\Psi}_{n+1} + \hat{\Psi}_{n+1}^\dagger \mathbf{T}_n^{(e)\dagger} \hat{\Psi}_n \right) \right\}, \\ \mathbf{V}_n^{(o)} &= v_{n,1} \sigma_1 + v_{n,2} \sigma_2 + v_{n,3} \sigma_3, \\ \mathbf{U}_n^{(e)} &= U_{n,0} \sigma_0, \\ \mathbf{T}_n^{(e)} &= t'_{n,0} \sigma_0 + i (t''_{n,1} \sigma_1 + t''_{n,2} \sigma_2 + t''_{n,3} \sigma_3), \end{aligned} \quad (\text{A7b})$$

TABLE II. The first three tables from left to right give the transformation laws of $\sigma_\mu \otimes \tau_\nu$ with $\mu, \nu = 0, \dots, 3$ under complex conjugation $*$, multiplication from the left and from the right by $\sigma_2 \otimes \tau_0$, and by composition of the two operations, respectively.

	τ_0	τ_1	τ_2	τ_3		τ_0	τ_1	τ_2	τ_3		τ_0	τ_1	τ_2	τ_3
σ_0	+	+	-	+	σ_0	+	+	+	+	σ_0	+	+	-	+
σ_1	+	+	-	+	σ_1	-	-	-	-	σ_1	-	-	+	-
σ_2	-	-	+	-	σ_2	+	+	+	+	σ_2	-	-	+	-
σ_3	+	+	-	+	σ_3	-	-	-	-	σ_3	-	-	+	-

is even under the transformation (A5b), while

$$\begin{aligned} \hat{H}^{(o)} &= \int_{\text{edge}} dx \sum_{n=1}^{2N} \left\{ \hat{\Psi}_n^\dagger \left[V_n^{(e)} (-i) \partial_x + U_n^{(o)} \right] \hat{\Psi}_n + \left(\hat{\Psi}_n^\dagger T_n^{(o)} \hat{\Psi}_{n+1} + \hat{\Psi}_{n+1}^\dagger T_n^{(o)\dagger} \hat{\Psi}_n \right) \right\}, \\ V_n^{(e)} &= v_{n,0} \sigma_0, \\ U_n^{(o)} &= U_{n,1} \sigma_1 + U_{n,2} \sigma_2 + U_{n,3} \sigma_3, \\ T_n^{(o)} &= t'_{n,1} \sigma_1 + t'_{n,2} \sigma_2 + t'_{n,3} \sigma_3 + i t''_{n,0} \sigma_0, \end{aligned} \quad (\text{A7c})$$

is odd under the transformation (A5b).

b. Gauge transformation

We do the gauge transformation

$$\hat{\Psi}_n^\dagger \rightarrow (+i)^n \hat{\Psi}_n^\dagger, \quad \hat{\Psi}_n \rightarrow (-i)^n \hat{\Psi}_n. \quad (\text{A8})$$

Under this gauge transformation

$$\hat{H} := \int_{\text{edge}} dx \sum_{n=1}^{2N} \left\{ \hat{\Psi}_n^\dagger [V_n (-i) \partial_x + U_n] \hat{\Psi}_n + (-i) \left(\hat{\Psi}_n^\dagger T_n \hat{\Psi}_{n+1} - \hat{\Psi}_{n+1}^\dagger T_n^\dagger \hat{\Psi}_n \right) \right\}, \quad (\text{A9a})$$

while the operation (A5b) of time reversal reads

$$\hat{\Psi}_n^\dagger(x) = \hat{\Psi}_n^{\prime\dagger}(x) K \sigma_2 (-i)^n, \quad \hat{\Psi}_n(x) = (+i)^n \sigma_2 K \hat{\Psi}_n'(x). \quad (\text{A9b})$$

c. Preparation for the continuum limit in the stacking direction

The continuum limit in the stacking direction consists in doing the replacements

$$\begin{aligned} \hat{\Psi}_{2n}(x) &\rightarrow (2\mathbf{a}_y)^{1/2} \hat{\eta}_1(x, y), & \hat{\Psi}_{2n\pm 2}(x) &\rightarrow (2\mathbf{a}_y)^{1/2} \left[\hat{\eta}_1(x, y) \pm (2\mathbf{a}_y) \left(\frac{\partial \hat{\eta}_1}{\partial y} \right) (x, y) + \dots \right], \\ \hat{\Psi}_{2n+1}(x) &\rightarrow (2\mathbf{a}_y)^{1/2} \hat{\eta}_2(x, y), & \hat{\Psi}_{2n+1\pm 2}(x) &\rightarrow (2\mathbf{a}_y)^{1/2} \left[\hat{\eta}_2(x, y) \pm (2\mathbf{a}_y) \left(\frac{\partial \hat{\eta}_2}{\partial y} \right) (x, y) + \dots \right], \end{aligned} \quad (\text{A10a})$$

for the operators,

$$\left. \begin{aligned} V_{2n} &= V_+(x, y) + V_-(x, y) \\ V_{2n+1} &= V_+(x, y) - V_-(x, y) \end{aligned} \right\} \quad V_\pm(x, y) = V_\pm^\dagger(x, y) \quad (\text{A10b})$$

for the velocity matrices,

$$\left. \begin{aligned} U_{2n} &= U_+(x, y) + U_-(x, y) \\ U_{2n+1} &= U_+(x, y) - U_-(x, y) \end{aligned} \right\} \quad U_\pm(x, y) = U_\pm^\dagger(x, y) \quad (\text{A10c})$$

TABLE III. The three tables from left to right give the transformation laws of $\sigma_\mu \otimes \tau_\nu$ with $\mu, \nu = 0, \dots, 3$ under complex conjugation $*$, multiplication from the left and from the right by $\sigma_2 \otimes \tau_3$, and by composition of the two operations, respectively.

	τ_0	τ_1	τ_2	τ_3
σ_0	+	+	-	+
σ_1	+	+	-	+
σ_2	-	-	+	-
σ_3	+	+	-	+

	τ_0	τ_1	τ_2	τ_3
σ_0	+	-	-	+
σ_1	-	+	+	-
σ_2	+	-	-	+
σ_3	-	+	+	-

	τ_0	τ_1	τ_2	τ_3
σ_0	+	-	+	+
σ_1	-	+	-	-
σ_2	-	+	-	-
σ_3	-	+	-	-

for the on-site potential matrices,

$$\begin{aligned}
\mathbb{T}_{2n} &= W_+(x, y) + W_-(x, y), & \mathbb{T}_{2n}^\dagger &= W_+^\dagger(x, y) + W_-^\dagger(x, y), \\
\mathbb{T}_{2n+1} &= W_+(x, y) - W_-(x, y) + (2\mathbf{a}_y) (\partial_y W_+) (x, y) - (2\mathbf{a}_y) (\partial_y W_-) (x, y), \\
\mathbb{T}_{2n-1}^\dagger &= W_+^\dagger(x, y) - W_-^\dagger(x, y) - (2\mathbf{a}_y) (\partial_y W_+^\dagger) (x, y) + (2\mathbf{a}_y) (\partial_y W_-^\dagger) (x, y),
\end{aligned} \tag{A10d}$$

for the tunneling matrices, and

$$\sum_{n=1}^N (2\mathbf{a}_y) \equiv \int_0^{N(2\mathbf{a}_y)} dy \tag{A10e}$$

once the continuum limit has been taken. In anticipation of the continuum limit, we shall already use Eq. (A10e).

With the help of the compacter notation

$$\hat{\chi} := \begin{pmatrix} \hat{\eta}_1 \\ \hat{\eta}_2 \end{pmatrix} \tag{A11a}$$

and the decomposition

$$A = \frac{A + A^\dagger}{2} + i \left(\frac{A - A^\dagger}{2i} \right) \equiv \text{Re } A + i \text{Im } A \tag{A11b}$$

of any matrix A into its real and imaginary parts $\text{Re } A = (\text{Re } A)^\dagger$ and $\text{Im } A = (\text{Im } A)^\dagger$, respectively, we find that, with the help of Table III, we may decompose the expansion up to first order in powers of \mathbf{a}_y of the single-particle Hamiltonian (A9a) into its even and odd contributions under reversal of time (A9b) according to

$$\hat{H} = \int_{edge} dx \int_0^{N(2\mathbf{a}_y)} dy \mathcal{H}(x, y), \quad \mathcal{H}(x, y) = \mathcal{H}^{(e)}(x, y) + \mathcal{H}^{(o)}(x, y). \tag{A11c}$$

Here, we need to introduce the unit 2×2 matrix τ_0 and the Pauli matrices τ_1 , τ_2 , and τ_3 with the help of which

$$\begin{aligned}
\mathcal{H}^{(e)}(x, y) &= \left[V_+^{(o,0)}(x, y) \otimes \tau_0 + V_-^{(o,3)}(x, y) \otimes \tau_3 \right] (-i) \partial_x \\
&+ U_+^{(e,0)}(x, y) \otimes \tau_0 + U_-^{(e,3)}(x, y) \otimes \tau_3 \\
&+ 2 (\text{Im } W_+)^{(e,1)}(x, y) \otimes \tau_1 + 2 (\text{Re } W_-)^{(e,2)}(x, y) \otimes \tau_2 \\
&+ (2\mathbf{a}_y) \left\{ (-i) \partial_y \left[\text{Re} (W_+^\dagger - W_-^\dagger) \right]^{(o,1)}(x, y) \otimes \tau_1 - (-i) \partial_y \left[\text{Im} (W_+^\dagger - W_-^\dagger) \right]^{(o,2)}(x, y) \otimes \tau_2 \right\} \\
&+ (2\mathbf{a}_y) \left\{ \left[\text{Re} (W_+^\dagger - W_-^\dagger) \right]^{(o,1)}(x, y) \otimes \tau_1 (-i) \partial_y - \left[\text{Im} (W_+^\dagger - W_-^\dagger) \right]^{(o,2)}(x, y) \otimes \tau_2 (-i) \partial_y \right\}
\end{aligned} \tag{A11d}$$

and

$$\begin{aligned}
\mathcal{H}^{(o)}(x, y) = & \left[V_+^{(e,0)}(x, y) \otimes \tau_0 + V_-^{(e,3)}(x, y) \otimes \tau_3 \right] (-i) \partial_x \\
& + U_+^{(o,0)}(x, y) \otimes \tau_0 + U_-^{(o,3)}(x, y) \otimes \tau_3 \\
& + 2 (\text{Im } W_+)^{(o,1)}(x, y) \otimes \tau_1 + 2 (\text{Re } W_-)^{(o,2)}(x, y) \otimes \tau_2 \\
& + (2\mathbf{a}_y) \left\{ (-i) \partial_y \left[\text{Re} \left(W_+^\dagger - W_-^\dagger \right) \right]^{(e,1)}(x, y) \otimes \tau_1 - (-i) \partial_y \left[\text{Im} \left(W_+^\dagger - W_-^\dagger \right) \right]^{(e,2)}(x, y) \otimes \tau_2 \right\} \\
& + (2\mathbf{a}_y) \left\{ \left[\text{Re} \left(W_+^\dagger - W_-^\dagger \right) \right]^{(e,1)}(x, y) \otimes \tau_1 (-i) \partial_y - \left[\text{Im} \left(W_+^\dagger - W_-^\dagger \right) \right]^{(e,2)}(x, y) \otimes \tau_2 (-i) \partial_y \right\}.
\end{aligned} \tag{A11e}$$

For any $A := a_\mu \sigma_\mu = A^\dagger$ with $a_\mu \in \mathbb{R}$ for $\mu = 0, 1, 2, 3$, the notation

$$A \otimes \tau_\nu = A^{(e,\nu)} \otimes \tau_\nu + A^{(o,\nu)} \otimes \tau_\nu \tag{A11f}$$

is defined by demanding that

$$\begin{aligned}
\text{for } A^{(e,\nu)} \otimes \tau_\nu, \quad \sigma_2 \otimes \tau_3 \left(A^{(e,\nu)} \otimes \tau_\nu \right)^* \sigma_2 \otimes \tau_3 &= +A^{(e,\nu)} \otimes \tau_\nu, \\
\text{for } A^{(o,\nu)} \otimes \tau_\nu, \quad \sigma_2 \otimes \tau_3 \left(A^{(o,\nu)} \otimes \tau_\nu \right)^* \sigma_2 \otimes \tau_3 &= -A^{(o,\nu)} \otimes \tau_\nu,
\end{aligned} \tag{A11g}$$

hold for any $\nu = 0, 1, 2, 3$.

d. Continuum limit that delivers the Dirac Hamiltonian when time-reversal symmetry holds

We specialize to the case when time-reversal symmetry holds. In other words, we seek a well-defined continuum limit for the single-particle Hamiltonian

$$\begin{aligned}
\mathcal{H}^{(e)}(x, y) = & \left[V_+^{(o,0)}(x, y) \otimes \tau_0 + V_-^{(o,3)}(x, y) \otimes \tau_3 \right] (-i) \partial_x \\
& + U_+^{(e,0)}(x, y) \otimes \tau_0 + U_-^{(e,3)}(x, y) \otimes \tau_3 \\
& + 2 (\text{Im } W_+)^{(e,1)}(x, y) \otimes \tau_1 + 2 (\text{Re } W_-)^{(e,2)}(x, y) \otimes \tau_2 \\
& + (2\mathbf{a}_y) \left\{ (-i) \partial_y \left[\text{Re} \left(W_+^\dagger - W_-^\dagger \right) \right]^{(o,1)}(x, y) \otimes \tau_1 - (-i) \partial_y \left[\text{Im} \left(W_+^\dagger - W_-^\dagger \right) \right]^{(o,2)}(x, y) \otimes \tau_2 \right\} \\
& + (2\mathbf{a}_y) \left\{ \left[\text{Re} \left(W_+^\dagger - W_-^\dagger \right) \right]^{(o,1)}(x, y) \otimes \tau_1 (-i) \partial_y - \left[\text{Im} \left(W_+^\dagger - W_-^\dagger \right) \right]^{(o,2)}(x, y) \otimes \tau_2 (-i) \partial_y \right\},
\end{aligned} \tag{A12a}$$

where the symmetry under conjugation by $\sigma_2 \otimes \tau_3 K$ (K complex conjugation) implies that (see Table III)

$$\begin{aligned}
V_+^{(o,0)} &= v_{+,j} \sigma_j, & V_-^{(o,3)} &= v_{-,j} \sigma_j, & v_{\pm,j} &\in \mathbb{R}, & j &= 1, 2, 3, \\
U_+^{(e,0)} &= u_{+,0} \sigma_0, & U_-^{(e,3)} &= u_{-,0} \sigma_0, & u_{\pm,0} &\in \mathbb{R}, \\
(\text{Im } W_+)^{(e,1)} &= w''_{+,j} \sigma_j, & (\text{Re } W_-)^{(e,2)} &= w'_{-,0} \sigma_0, \\
\left[\text{Re} \left(W_+^\dagger - W_-^\dagger \right) \right]^{(o,1)} &= + (w'_{+,0} - w'_{-,0}) \sigma_0, & \left[\text{Im} \left(W_+^\dagger - W_-^\dagger \right) \right]^{(o,2)} &= - (w''_{+,j} - w''_{-,j}) \sigma_j.
\end{aligned} \tag{A12b}$$

Recall here that, for any $\nu = 0, 1, 2, 3$, evenness or oddness under time-reversal is not imposed on the 4×4 complex matrices

$$W_\pm \otimes \tau^\nu \equiv (w'_{\pm,\mu} \sigma_\mu + i w''_{\pm,\mu} \sigma_\mu) \otimes \tau^\nu, \quad w'_{\pm,\mu}, w''_{\pm,\mu} \in \mathbb{R}, \quad \mu = 0, 1, 2, 3, \tag{A13}$$

but on their real and imaginary parts

$$(\text{Re } W_\pm) \otimes \tau^\nu = w'_{\pm,\mu} \sigma_\mu \otimes \tau^\nu, \quad (\text{Im } W_\pm) \otimes \tau^\nu = w''_{\pm,\mu} \sigma_\mu \otimes \tau^\nu, \tag{A14}$$

respectively.

The continuum limit involves the limit $\mathbf{a}_y \rightarrow 0$. To make sense of this limit on the two last lines of the right-hand side of Eq. (A12a), we first assume the additive decompositions into a constant (denoted by a straight overline) and position dependent (denoted by a wiggly overline),

$$v_{\pm,\mu}(x, y) = \bar{v}_{\pm,\mu} + \tilde{v}_{\pm,\mu}(x, y) \quad (\text{A15a})$$

for the “Fermi velocities”

$$u_{\pm,\mu}(x, y) = \bar{u}_{\pm,\mu} + \tilde{u}_{\pm,\mu}(x, y) \quad (\text{A15b})$$

for the on-site potentials, and

$$w'_{\pm,\mu}(x, y) = \bar{w}'_{\pm,\mu} + \tilde{w}'_{\pm,\mu}(x, y), \quad w''_{\pm,0}(x, y) = \bar{w}''_{\pm,0} + \tilde{w}''_{\pm,0}(x, y), \quad (\text{A15c})$$

for the tunneling amplitudes. All the wiggly fields are smooth functions, i.e., their y derivatives are assumed to be of order $(\mathbf{a}_y)^0 = 1$. Second, we take the limit of infinite band width along the y direction by which

$$\bar{w}'_{+,0} \times (2\mathbf{a}_y) \equiv v_{u,y} \quad (\text{A16a})$$

is held fixed to a non-vanishing and positive number as $\bar{w}'_{+,0} \rightarrow \infty$ and $\mathbf{a}_y \rightarrow 0$ [recall Eq. (A4b)], whereas

$$\frac{v_{\pm,j}(x, y)}{\bar{w}'_{+,0}}, \frac{u_{\pm,0}(x, y)}{\bar{w}'_{+,0}}, \frac{w'_{-,0}(x, y)}{\bar{w}'_{+,0}}, \frac{w''_{\pm,j}(x, y)}{\bar{w}'_{+,0}} \rightarrow 0, \quad j = 1, 2, 3, \quad (\text{A16b})$$

in the same limit for any $(x, y) \in \mathbb{R}^2$. Consequently, the penultimate line and the last line, except for the term $v_{u,y} \sigma_0 \otimes \tau_1 (-i) \partial_y$, on the right-hand side of Eq. (A12a) vanish in this limit. Third, we assume for simplicity but without loss of generality that

$$\bar{v}_{-,3} \equiv v_{s,x} \quad (\text{A17a})$$

is a finite and non-vanishing positive number, while

$$\bar{v}_{+,j} = \bar{v}_{-,1} = \bar{v}_{-,2} = 0, \quad j = 1, 2, 3. \quad (\text{A17b})$$

Fourth, we consider the limit

$$\frac{\tilde{v}_{\pm,\mu}(x, y)}{v_{s,x}} \rightarrow 0, \quad \mu = 0, 1, 2, 3, \quad (\text{A18})$$

for any $(x, y) \in \mathbb{R}^2$. This limit justifies treating a Dirac point as a fixed point in the sense of the renormalization group. Fifth, we assume a finite and non-vanishing dimerization

$$\bar{w}'_{-,0} \neq 0, \infty. \quad (\text{A19})$$

The Dirac point is then captured by the single-particle Hamiltonian

$$\begin{aligned} \mathcal{H}_D^{\text{AI}} &\equiv \bar{\mathcal{H}}^{(\text{e})} \\ &= v_{s,x} \sigma_3 \otimes \tau_3 (-i) \partial_x + v_{u,y} \sigma_0 \otimes \tau_1 (-i) \partial_y \\ &\quad + \bar{u}_{+,0} \sigma_0 \otimes \tau_0 + \bar{u}_{-,0} \sigma_0 \otimes \tau_3 + 2 \bar{w}''_{+,j} \sigma_j \otimes \tau_1 + 2 \bar{w}'_{-,0} \sigma_0 \otimes \tau_2. \end{aligned} \quad (\text{A20})$$

The parameters $v_{s,x}$ and $v_{u,y}$ enter as anisotropic Dirac velocities. The parameter $\bar{u}_{+,0}$ enters as a chemical potential. The parameter $2 \bar{w}'_{-,0}$ enters as a mass. It anticommutes with all terms except for the chemical potential. The remaining 4 parameters $\bar{u}_{-,0}$ and $\bar{w}''_{+,j}$ with $j = 1, 2, 3$ do not anticommute with all the gamma matrices multiplying the first derivatives in position space.

Appendix B: Dirac Hamiltonian from the two-dimensional spin-directed \mathbb{Z}_2 network model

Starting from the two-dimensional CC network model, Ho and Chalker derived in Ref. 82 the random Dirac Hamiltonian studied in Ref. 83 on its own merits. The two-dimensional \mathbb{Z}_2 network model for a strong two-dimensional \mathbb{Z}_2 topological insulator was related to a random Dirac Hamiltonian in Ref. 44. In this Appendix, we derive from the two-dimensional spin-directed \mathbb{Z}_2 network model a random Dirac Hamiltonian.

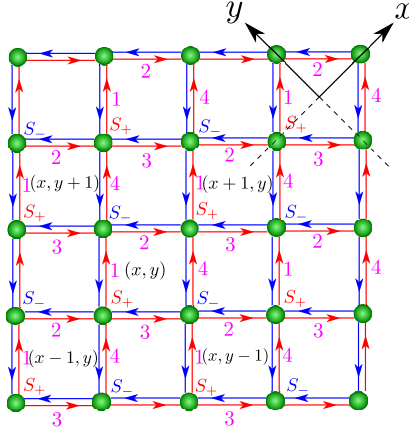


FIG. 18. (Color online:) The vertex representation in Fig. 6(a) of the two-dimensional spin-directed \mathbb{Z}_2 network model is displayed after rotating counterclockwise Fig. 6(a) by $\pi/4$. The vertices at which the elementary scattering shown in Fig. 5 takes place form a bipartite square lattice denoted Λ . Each of the two interpenetrating sublattices of Λ is a square lattice. They are denoted Λ_+ and Λ_- . The vertices of sublattices Λ_+ represent the scattering matrix S_+ obtained from Eq. (2.3) with the substitution $t \rightarrow t_+$ and $r \rightarrow r_+$. The vertices of sublattices Λ_- represent the scattering matrix S_- obtained from Eq. (2.3) with the substitution $t \rightarrow t_-$ and $r \rightarrow r_-$. The lattice dual to Λ , denoted Λ^* , is made of the sites at the center of the plaquettes of Λ . The four edges of a plaquette of Λ are either numbered 3, 4, 2, 1 or 2, 1, 3, 4 in a counterclockwise fashion. The sites of Λ^* denoted (x, y) are the centers of the plaquettes from Λ numbered 3, 4, 2, 1 counterclockwise. This leaves all the sites of Λ^* unnumbered if they are centers of plaquettes in Λ numbered 2, 1, 3, 4 counterclockwise. Pairs of helical plane waves that form a Kramers' degenerate doublet are represented by arrows on the nearest-neighbor links of Λ . The color code is red for spin up and blue for spin down. The eight plane waves along the edges of the plaquette centered on the site (x, y) from the dual lattice Λ^* are assigned the coordinate (x, y) .

1. Block-off-diagonal representation of the scattering matrix

To this end and along the same lines as in Ref. 44, we are going to reformulate the two-dimensional spin-directed \mathbb{Z}_2 network model in a form more suitable for taking a continuum limit that will yield a Dirac Hamiltonian.

With the notations and conventions explained in Fig. 18, we can drop the incoming and outgoing labels on the plane waves in an unambiguous way and write, for example,

$$\psi_{1,\uparrow}(x, y) = e^{+i\phi_0} [r_+ e^{+i\phi_3} \psi_{2,\uparrow}(x-1, y) + t_+ e^{+i\phi_1} \cos \theta \psi_{4,\uparrow}(x-1, y) + t_+ e^{+i\phi_2} \sin \theta \psi_{3,\downarrow}(x, y)] \quad (\text{B1a})$$

and (we need to make the identification $S^\dagger \rightarrow S_-$)

$$\psi_{1,\downarrow}(x, y) = e^{-i\phi_0} [r_- e^{-i\phi_3} \psi_{2,\downarrow}(x, y) - t_- e^{-i\phi_2} \sin \theta \psi_{3,\uparrow}(x, y+1) + t_- e^{+i\phi_1} \cos \theta \psi_{4,\downarrow}(x, y+1)]. \quad (\text{B1b})$$

Carrying the same manipulations for edges 2, 3, and 4 of the plaquette centered at (x, y) in the dual lattice of Fig. 18, suggests the introduction of the eight-component spinor

$$\Psi(x, y) := \begin{pmatrix} \Psi_+(x, y) \\ \Psi_-(x, y) \end{pmatrix}, \quad \Psi_+(x, y) := \begin{pmatrix} \psi_{1,\uparrow}(x, y) \\ \psi_{4,\downarrow}(x, y) \\ \psi_{3,\uparrow}(x, y) \\ \psi_{2,\downarrow}(x, y) \end{pmatrix}, \quad \Psi_-(x, y) := \begin{pmatrix} \psi_{1,\downarrow}(x, y) \\ \psi_{4,\uparrow}(x, y) \\ \psi_{3,\downarrow}(x, y) \\ \psi_{2,\uparrow}(x, y) \end{pmatrix}, \quad (\text{B2a})$$

the 8×8 operator-valued matrix

$$\hat{S} := \begin{pmatrix} 0 & \hat{S}_{+-} \\ \hat{S}_{-+} & 0 \end{pmatrix}, \quad (\text{B2b})$$

where the 4×4 operator-valued matrices are given by

$$\hat{S}_{+-} := e^{+i\phi_0} \begin{pmatrix} 0 & t_+ e^{+i\phi_1} \cos \theta \hat{s}_-^x & t_+ e^{+i\phi_2} \sin \theta & r_+ e^{+i\phi_3} \hat{s}_-^x \\ t_+ e^{+i\phi_1} \cos \theta \hat{s}_+^x & 0 & r_+ e^{-i\phi_3} \hat{s}_+^x & -t_+ e^{-i\phi_2} \sin \theta \\ -t_+ e^{+i\phi_2} \sin \theta & r_+ e^{-i\phi_3} \hat{s}_-^x & 0 & -t_+ e^{-i\phi_1} \cos \theta \hat{s}_-^x \\ r_+ e^{+i\phi_3} \hat{s}_+^x & t_+ e^{-i\phi_2} \sin \theta & -t_+ e^{-i\phi_1} \cos \theta \hat{s}_+^x & 0 \end{pmatrix} \quad (\text{B2c})$$

and

$$\hat{S}_{-+} := e^{+i\phi'_0} \begin{pmatrix} 0 & +t_- e^{+i\phi'_1} \cos \theta \hat{s}_+^y & -t_- e^{-i\phi'_2} \sin \theta \hat{s}_+^y & r_- e^{-i\phi'_3} \\ t_- e^{+i\phi'_1} \cos \theta \hat{s}_-^y & 0 & r_- e^{+i\phi'_3} & t_- e^{+i\phi'_2} \sin \theta \hat{s}_-^y \\ t_- e^{-i\phi'_2} \sin \theta \hat{s}_-^y & r_- e^{+i\phi'_3} & 0 & -t_- e^{-i\phi'_1} \cos \theta \hat{s}_-^y \\ r_- e^{-i\phi'_3} & -t_- e^{+i\phi'_2} \sin \theta \hat{s}_+^y & -t_- e^{-i\phi'_1} \cos \theta \hat{s}_+^y & 0 \end{pmatrix}, \quad (\text{B2d})$$

while we have introduced the translation operators

$$(\hat{s}_\pm^x f)(x, y) = f(x \pm 1, y), \quad (\hat{s}_\pm^y f)(x, y) = f(x, y \pm 1), \quad (\text{B2e})$$

for we may then interpret the linear equation

$$\Psi(x, y; t + \delta t) := \hat{\mathcal{U}} \Psi(x, y; t), \quad \hat{\mathcal{U}} := \hat{S}^2 = \begin{pmatrix} \hat{S}_{+-} & \hat{S}_{-+} & 0 \\ 0 & \hat{S}_{-+} & \hat{S}_{+-} \end{pmatrix} = \hat{\mathcal{U}}^\dagger, \quad (\text{B2f})$$

as a unitary time-evolution by the discrete time step $\delta t \equiv 1$ for the two-dimensional spin-directed \mathbb{Z}_2 network model. Following Ho and Chalker,⁸² we may define the Hamiltonian

$$\hat{\mathcal{H}} := +i(\hat{\mathcal{U}} - 1) \equiv \begin{pmatrix} \hat{H}_{+-} & 0 \\ 0 & \hat{H}_{-+} \end{pmatrix} \quad (\text{B3})$$

for the two-dimensional spin-directed \mathbb{Z}_2 network model. Without loss of generality, we are after the upper 4×4 Hermitean block

$$\hat{H}_{+-} \equiv \begin{pmatrix} \hat{H}_A & \hat{H}_{AB} \\ \hat{H}_{AB}^\dagger & \hat{H}_B \end{pmatrix}, \quad \hat{H}_A = \hat{H}_A^\dagger, \quad \hat{H}_B = \hat{H}_B^\dagger, \quad (\text{B4})$$

for the two-dimensional spin-directed \mathbb{Z}_2 network model. In particular, we seek a continuum limit of \hat{H}_{+-} .

2. Dirac Hamiltonian from the two-dimensional spin-directed \mathbb{Z}_2 network model close to $\theta = \pi/2$

We are going to deduce Hamiltonian (B4) from expanding Eq. (B3) when the parameters of the two-dimensional spin-directed \mathbb{Z}_2 network model are in the close vicinity to the line that is parametrized by t^2 in the three-dimensional parameter space (2.7) and given by

$$(t^2, \theta, \delta^2) = (t^2, \pi/2, 0). \quad (\text{B5})$$

We have seen in Sec. II C 4 that the two-dimensional spin-directed \mathbb{Z}_2 network model decouples along this line into two critical CC network models. In turn, the critical CC network model is related to a Dirac Hamiltonian.⁸² For this reason we seek the continuum limit of Hamiltonian (B4) close to the critical line (B5).

The expansions

$$\begin{aligned} e^{+i\phi_0} &= 1 + i\phi_0 + \dots, & e^{+i\phi_1} &= 1 + i\phi_1 + \dots, & e^{+i\phi_2} &= 1 + i\phi_2 + \dots, & e^{+i\phi_3} &= 1 + i\phi_3 + \dots, \\ e^{+i\phi'_0} &= 1 + i\phi'_0 + \dots, & e^{+i(\pi+\phi'_1)} &= -(1 + i\phi'_1 + \dots), & e^{+i\phi'_2} &= 1 + i\phi'_2 + \dots, & e^{+i\phi'_3} &= 1 + i\phi'_3 + \dots, \end{aligned} \quad (\text{B6a})$$

for the random phases, the expansions

$$t_+ t_- = t^2 + \dots, \quad r_+ r_- = r^2 + \dots, \quad t_\pm r_\mp = t r \pm \frac{\delta^2}{2tr} + \dots, \quad \cos\left(\frac{\pi}{2} - \theta'\right) = \theta' + \dots, \quad \sin\left(\frac{\pi}{2} - \theta'\right) = 1 + \dots, \quad (\text{B6b})$$

for the products of the transmission and reflection amplitudes and for the deviations of θ about $\pi/2$ ($\theta = \frac{\pi}{2} - \theta'$), and the gradient expansions

$$s_\pm^x = 1 \pm \partial_x + \dots, \quad s_\pm^y = 1 \pm \partial_y + \dots, \quad (\text{B6c})$$

for the shift operators, deliver the following continuum limit for the three 2×2 blocks entering the right-hand side of Eq. (B4). With the notations

$$p_{x,y} \equiv -i\partial_{x,y}, \quad m \equiv \frac{\delta^2}{tr}, \quad A_x \equiv \phi_3 - \phi'_3, \quad A_y \equiv \phi_2 - \phi'_2, \quad \lambda_\phi \equiv \phi_1 - \phi'_1, \quad V_0 \equiv -\phi_0 - \phi'_0, \quad (\text{B7a})$$

one verifies that

$$\begin{aligned} \hat{H}_A &= -tr [(p_x - A_x) - (p_y - A_y)] \sigma_1 - m \sigma_2 + [r^2 (p_x - A_x) + t^2 (p_y - A_y)] \sigma_3, \\ \hat{H}_B &= +tr [(p_x + A_x) + (p_y + A_y)] \sigma_1 + m \sigma_2 + [r^2 (p_x + A_x) - t^2 (p_y + A_y)] \sigma_3, \\ \hat{H}_{AB} &= +\theta' t (2 + i\lambda_\phi) (ir \sigma_0 - t \sigma_2). \end{aligned} \quad (\text{B7b})$$

Since we assume that θ' is small, we neglect the other small variables, except for ϕ_1 and ϕ'_1 , to derive \hat{H}_{AB} . With the help of a second set of Pauli matrices τ_1 , τ_2 , and τ_3 , together with the unit 2×2 matrix τ_0 and the unitary transformation defined by

$$R(t) := \left(\sigma_0 \otimes \frac{\tau_0 + \tau_3}{2} + e^{-i\alpha(t)\sigma_2} \otimes \frac{\tau_0 - \tau_3}{2} \right) (e^{-i\frac{\pi}{4}\sigma_1} e^{-i\frac{\pi}{2}\sigma_2}) \otimes \tau_0, \quad \alpha(t) := \arcsin t, \quad (\text{B8a})$$

we find

$$\begin{aligned} \hat{H}_{+-} &= [tr (p_x - p_y) \sigma_1 + (r^2 p_x + t^2 p_y) \sigma_2] \otimes \tau_0 - [tr (A_x - A_y) \sigma_1 + (r^2 A_x + t^2 A_y) \sigma_2] \otimes \tau_3 \\ &\quad - m \sigma_3 \otimes \tau_3 - \theta' t (\lambda_\phi \sigma_0 \otimes \tau_1 + 2 \sigma_0 \otimes \tau_2) + V_0 \sigma_0 \otimes \tau_0. \end{aligned} \quad (\text{B8b})$$

This Hamiltonian is invariant under reversal of time, i.e.,

$$\mathcal{T} \hat{H}_{+-} \mathcal{T}^{-1} = \hat{H}_{+-}, \quad \mathcal{T} := i\sigma_2 \otimes \tau_1 \mathcal{K}, \quad (\text{B9})$$

where \mathcal{K} denotes the operation of complex conjugation. The mass m that encodes the dimerization multiplies the matrix $\sigma_3 \otimes \tau_3$ that anticommutes with all other contributions to the continuum limit (B8b) with $V_0 = 0$. Hence, dimerization opens a spectral gap in the spectrum of Hamiltonian (B8b). At the isotropic point defined by $t^2 = r^2 = 1/2$, Hamiltonian (B8b) becomes the Dirac Hamiltonian

$$\hat{H}_{+-} = \frac{1}{\sqrt{2}} (p'_x \sigma_1 + p'_y \sigma_2) \otimes \tau_0 - \frac{1}{\sqrt{2}} (A'_x \sigma_1 + A'_y \sigma_2) \otimes \tau_3 - m \sigma_3 \otimes \tau_3 - \frac{\theta'}{\sqrt{2}} (\lambda_\phi \sigma_0 \otimes \tau_1 + 2 \sigma_0 \otimes \tau_2) + V_0 \sigma_0 \otimes \tau_0, \quad (\text{B10a})$$

where

$$p'_x \equiv \frac{p_x - p_y}{\sqrt{2}}, \quad p'_y \equiv \frac{p_x + p_y}{\sqrt{2}}, \quad A'_x \equiv \frac{A_x - A_y}{\sqrt{2}}, \quad A'_y \equiv \frac{A_x + A_y}{\sqrt{2}}. \quad (\text{B10b})$$

3. Dirac Hamiltonian from the two-dimensional spin-directed \mathbb{Z}_2 network model close to $\theta = 0$

We are going to deduce Hamiltonian (B4) from expanding Eq. (B3) when the parameters of the two-dimensional spin-directed \mathbb{Z}_2 network model are in the close vicinity to the line that is parametrized by t^2 in the three-dimensional parameter space (2.7) and given by

$$(t^2, \theta, \delta^2) = (t^2, 0, 0). \quad (\text{B11})$$

We have seen in Sec. IIC 2 that the two-dimensional spin-directed \mathbb{Z}_2 network model decouples along this line into two two-dimensional directed CC network model. In turn, the two-dimensional directed CC network model is critical. For this reason we seek the continuum limit of Hamiltonian (B4) close to the line (B11).

The spin up and down quantum numbers are separately conserved along the line (B11). This suggests the use of the basis for the scattering states defined by

$$\begin{pmatrix} \psi_{1,\uparrow}(x, y) \\ \psi_{3,\uparrow}(x, y) \\ \psi_{2,\downarrow}(x, y) \\ \psi_{4,\downarrow}(x, y) \end{pmatrix} = \hat{S}_{+-} \begin{pmatrix} \psi_{1,\downarrow}(x, y) \\ \psi_{3,\downarrow}(x, y) \\ \psi_{2,\uparrow}(x, y) \\ \psi_{4,\uparrow}(x, y) \end{pmatrix}, \quad \begin{pmatrix} \psi_{1,\downarrow}(x, y) \\ \psi_{3,\downarrow}(x, y) \\ \psi_{2,\uparrow}(x, y) \\ \psi_{4,\uparrow}(x, y) \end{pmatrix} = \hat{S}_{-+} \begin{pmatrix} \psi_{1,\uparrow}(x, y) \\ \psi_{3,\uparrow}(x, y) \\ \psi_{2,\downarrow}(x, y) \\ \psi_{4,\downarrow}(x, y) \end{pmatrix}. \quad (\text{B12})$$

The expansions

$$\begin{aligned} e^{+i\phi_0} &= 1 + i\phi_0 + \dots, & e^{+i\phi_1} &= 1 + i\phi_1 + \dots, & e^{+i\phi_2} &= 1 + i\phi_2 + \dots, & e^{+i\phi_3} &= 1 + i\phi_3 + \dots, \\ e^{+i\phi'_0} &= 1 + i\phi'_0 + \dots, & e^{+i\phi'_1} &= 1 + i\phi'_1 + \dots, & e^{+i(\pi+\phi'_2)} &= -(1 + i\phi'_2 + \dots), & e^{+i\phi'_3} &= 1 + i\phi'_3 + \dots, \end{aligned} \quad (\text{B13a})$$

for the random phases, the expansions

$$t_+ t_- = t^2 + \dots, \quad r_+ r_- = r^2 + \dots, \quad t_\pm r_\mp = t r \pm \frac{\delta^2}{2t r} + \dots, \quad \cos \theta = 1 + \dots, \quad \sin \theta = \theta + \dots, \quad (\text{B13b})$$

for the products of the transmission and reflection amplitudes and for the deviations of θ about 0, and the gradient expansions

$$s_\pm^x = 1 \pm \partial_x + \dots, \quad s_\pm^y = 1 \pm \partial_y + \dots, \quad (\text{B13c})$$

for the shift operators, deliver the following continuum limit for the three 2×2 blocks entering the right-hand side of Eq. (B4) represented in the basis (B12). With the notations

$$p_{x,y} \equiv -i\partial_{x,y}, \quad m \equiv \frac{\delta^2}{t r}, \quad A_x \equiv \phi_3 - \phi'_3, \quad A_y \equiv \phi_1 - \phi'_1, \quad \lambda_\phi \equiv \phi_2 + \phi'_2, \quad V_0 \equiv -\phi_0 - \phi'_0, \quad (\text{B14a})$$

one verifies that

$$\begin{aligned} \hat{H}_A &= p_x \sigma_0 + t r [A_x + (p_y - A_y)] \sigma_1 - m \sigma_2 - [r^2 A_x - t^2 (p_y - A_y)] \sigma_3, \\ \hat{H}_B &= -p_x \sigma_0 - t r [A_x + (p_y + A_y)] \sigma_1 + m \sigma_2 - [r^2 A_x - t^2 (p_y + A_y)] \sigma_3, \\ \hat{H}_{AB} &= -\theta t (+2 + i\lambda_\phi) (it \sigma_0 + r \sigma_2). \end{aligned} \quad (\text{B14b})$$

Since we assume that θ is small, we neglect the other small variables, except for ϕ_2 and ϕ'_2 , to derive \hat{H}_{AB} . With the help of a second set of Pauli matrices τ_1 , τ_2 , and τ_3 , together with the unit 2×2 matrix τ_0 and the unitary transformation defined by

$$R(t) := \left(\sigma_0 \otimes \frac{\tau_0 - \tau_3}{2} + e^{+i\beta(t)\sigma_2} \otimes \frac{\tau_0 - \tau_3}{2} \right) e^{-i\frac{\pi}{4}\sigma_1} \otimes \tau_0, \quad \beta(t) := \arccos t, \quad (\text{B15a})$$

we find

$$\begin{aligned} \hat{H}_{+-} &= p_x \sigma_0 \otimes \tau_3 + (t r p_y \sigma_1 + t^2 p_y \sigma_2) \otimes \tau_0 + [t r (A_x - A_y) \sigma_1 - (r^2 A_x + t^2 A_y) \sigma_2] \otimes \tau_3 \\ &\quad + m \sigma_3 \otimes \tau_3 + \theta t (\lambda_\phi \sigma_0 \otimes \tau_1 + 2 \sigma_0 \otimes \tau_2) + V_0 \sigma_0 \otimes \tau_0. \end{aligned} \quad (\text{B15b})$$

This Hamiltonian is invariant under reversal of time, i.e.,

$$\mathcal{T} \hat{H}_{+-} \mathcal{T}^{-1} = \hat{H}_{+-}, \quad \mathcal{T} := i\sigma_2 \otimes \tau_1 \mathcal{K}, \quad (\text{B16})$$

where \mathcal{K} denotes the operation of complex conjugation.

As was the case for the continuum limit (B8b), the term $V_0 \sigma_0 \otimes \tau_0$ acts as a chemical potential, for it commutes with all contributions to the continuum limit (B15b). We shall set $V_0 = 0$ when deciding if a gap at energy 0 is opened by dimerization. In comparison to the continuum limit (B8b), the term $p_x \sigma_0 \otimes \tau_3$ has appeared that commutes with all contributions to the continuum limit (B15b) except for the term $\theta t (\lambda_\phi \sigma_0 \otimes \tau_1 + 2 \sigma_0 \otimes \tau_2)$. If we set $t = A_x = A_y = V_0 = 0$, we find the two (two-fold degenerate) gapless dispersions $|p_x \pm m|$. More generally, a branch of excitation is expected to cross the energy 0 at some m -dependent value of the momentum when $\theta = V_0 = 0$. As the coupling m is caused by dimerization, dimerization thus fails to open a gap if we set $\theta = V_0 = 0$. On the other hand, because the term $\theta t (\lambda_\phi \sigma_0 \otimes \tau_1 + 2 \sigma_0 \otimes \tau_2)$ anticommutes with both $m \sigma_3 \otimes \tau_3$ and $p_x \sigma_0 \otimes \tau_3$, we expect that a sufficiently large θ opens a gap for a given m .

¹ F. D. M. Haldane, Phys. Rev. Lett. **61**, 2015 (1988).

² D. J. Thouless, M. Kohmoto, M. P. Nightingale, and M. den Nijs, Phys. Rev. Lett. **49**, 405 (1982).

- ³ B. I. Halperin, Phys. Rev. B **25**, 2185 (1982).
- ⁴ C. L. Kane and E. J. Mele, Phys. Rev. Lett. **95**, 226801 (2005).
- ⁵ C. L. Kane and E. J. Mele, Phys. Rev. Lett. **95**, 146802 (2005).
- ⁶ H. Suzuura and T. Ando, Phys. Rev. Lett. **89**, 266603 (2002).
- ⁷ T. Ando and H. Suzuura, J. Phys. Soc. Jpn. **71**, 2753 (2002).
- ⁸ Y. Takane, J. Phys. Soc. Jpn. **73**, 9 (2004); **73**, 1430 (2004); **73**, 2366 (2004).
- ⁹ B. I. Halperin, Jpn. J. Appl. Phys. **26**, Suppl. 26-3, 1913 (1987).
- ¹⁰ J. T. Chalker and A. Dohmen, Phys. Rev. Lett. **75**, 4496 (1995).
- ¹¹ L. Balents and M. P. A. Fisher, Phys. Rev. Lett. **76**, 2782 (1996).
- ¹² Y.-B. Kim, Phys. Rev. B **53**, 16 420 (1996).
- ¹³ H. Mathur, Phys. Rev. Lett. **78**, 2429 (1997).
- ¹⁴ I. A. Gruzberg, N. Read, and S. Sachdev, Phys. Rev. B **55**, 10593 (1997), *ibid* **56**, 13218 (1997).
- ¹⁵ S. Cho, L. Balents, and M. P. A. Fisher, Phys. Rev. B **56**, 15814 (1997).
- ¹⁶ L. Balents, M. P. A. Fisher, M. R. Zirnbauer, Nucl. Phys. B **483**, 601 (1997).
- ¹⁷ D. P. Druist, P. J. Turley, K. D. Maranowski, E. G. Gwinn, and A. C. Gossard, Phys. Rev. Lett. **80**, 365 (1998).
- ¹⁸ L. Fu, C. L. Kane, and E. J. Mele, Phys. Rev. Lett. **98**, 106803 (2007).
- ¹⁹ J. E. Moore and L. Balents, Phys. Rev. B **75**, 121306(R) (2007).
- ²⁰ R. Roy, arXiv:cond-mat/0604211 (unpublished); Phys. Rev. B **79**, 195322 (2009).
- ²¹ L. Fu and C. L. Kane, Phys. Rev. B **76**, 045302 (2007).
- ²² D. Hsieh, D. Qian, L. Wray, Y. Xia, Y. S. Hor, R. J. Cava, and M. Z. Hasan, Nature **452**, 970 (2008).
- ²³ Y. Xia, L. Wray, D. Qian, D. Hsieh, A. Pal, H. Lin, A. Bansil, D. Grauer, Y. Hor, R. Cava, and M. Z. Hasan, Nature Physics **5**, 398 (2009).
- ²⁴ Y. L. Chen, J. G. Analytis, J. H. Chu, Z. K. Liu, S.-K. Mo, X. L. Qi, H. J. Zhang, D. H. Lu, X. Dai, Z. Fang, S. C. Zhang, I. R. Fisher, Z. Hussain, and Z.-X. Shen, Science **325**, 178 (2009).
- ²⁵ H. Lin, R. S. Markiewicz, L. A. Wray, L. Fu, M. Z. Hasan, and A. Bansil, Phys. Rev. Lett. **105**, 036404 (2010).
- ²⁶ T. Sato, K. Segawa, H. Guo, K. Sugawara, S. Souma, T. Takahashi, and Y. Ando, Phys. Rev. Lett. **105**, 136802 (2010).
- ²⁷ K. Kuroda, M. Ye, A. Kimura, S. V. Eremin, E. E. Krasovskii, E. V. Chulkov, Y. Ueda, K. Miyamoto, T. Okuda, K. Shimada, H. Namatame, and M. Taniguchi, Phys. Rev. Lett. **105**, 146801 (2010).
- ²⁸ Y. L. Chen, Z. K. Liu, J. G. Analytis, J.-H. Chu, H. J. Zhang, B. H. Yan, S.-K. Mo, R. G. Moore, D. H. Lu, I. R. Fisher, S. C. Zhang, Z. Hussain, and Z.-X. Shen, Phys. Rev. Lett. **105**, 266401 (2010).
- ²⁹ B. Rasche, A. Isaeva, M. Ruck, S. Borisenko, V. Zabolotnyy, B. Büchner, K. Koepf, C. Ortix, M. Richter, and J. van den Brink, Nature Materials **12**, 422 (2013).
- ³⁰ P. M. Ostrovsky, I. V. Gornyi, and A. D. Mirlin, Phys. Rev. Lett. **98**, 256801 (2007).
- ³¹ S. Ryu, C. Mudry, H. Obuse, and A. Furusaki, Phys. Rev. Lett. **99**, 116601 (2007).
- ³² The order of limits matters here. We assume that we can describe the disordered surface states of a strong \mathbb{Z}_2 topological insulator by a Dirac Hamiltonian in a two-dimensional representation of the Clifford algebra with all random potentials compatible with the time-reversal symmetry white-noise correlated. The disorder strength is measured by the variances g^2 of the random potentials. The strong disorder limit by which the variances g^2 are made arbitrarily large within the Dirac approximation presumes that $g \ll \Delta$ still holds whereby Δ is the bulk band gap. The opposite limit for which the disorder strength is larger than the bulk band gap destroys all topological attributes.
- ³³ J. H. Bardarson, J. Tworzydło, P. W. Brouwer, and C. W. J. Beenakker, Phys. Rev. Lett. **99**, 106801 (2007).
- ³⁴ K. Nomura, M. Koshino, and S. Ryu, Phys. Rev. Lett. **99**, 146806 (2007).
- ³⁵ C.-X. Liu, X.-L. Qi, and S.-C. Zhang, Physica E **44**, 906 (2012).
- ³⁶ R. S. K. Mong, J. H. Bardarson, and J. E. Moore, Phys. Rev. Lett. **108**, 076804 (2012).
- ³⁷ L. Fu and C. L. Kane, Phys. Rev. Lett. **109**, 246605 (2012).
- ³⁸ T. Morimoto and A. Furusaki, unpublished.
- ³⁹ C. Callan and J. A. Harvey, Nucl. Phys. B **250**, 427 (1985).
- ⁴⁰ Z. Ringel, Y. E. Kraus, and A. Stern, Phys. Rev. B **86**, 045102 (2012).
- ⁴¹ K. Kobayashi, T. Ohtsuki, and K.-I. Imura, Phys. Rev. Lett. **110**, 236803 (2013).
- ⁴² H. Obuse, A. Furusaki, S. Ryu, and C. Mudry, Phys. Rev. B **76**, 075301 (2007).
- ⁴³ H. Obuse, A. Furusaki, S. Ryu, and Christopher Mudry, Phys. Rev. B **78**, 115301 (2008).
- ⁴⁴ S. Ryu, C. Mudry, H. Obuse, and A. Furusaki, New J. Phys. **12**, 065005 (2010).
- ⁴⁵ V. M. Yakovenko, Phys. Rev. B **43**, 11353 (1991).
- ⁴⁶ D.-H. Lee, Phys. Rev. B **50**, 10788 (1994).
- ⁴⁷ C. L. Kane, R. Mukhopadhyay, and T. C. Lubensky, Phys. Rev. Lett. **88**, 036401 (2002).
- ⁴⁸ J. C. Teo and C. L. Kane, arXiv:1111.2617v1 [cond-mat.mes-hall].
- ⁴⁹ Critical transport in the direction orthogonal to the direction along which transport is perfect (directed) in the directed CC network model for a weak three-dimensional Chern insulator was established by Chalker and Dohmen in Ref. 10. They quantified how the transport along the direction that corresponds to the stacking direction of a weak three-dimensional Chern insulator depends on the ratio of the height and the perimeter in the cylindrical geometry of Fig. 2.
- ⁵⁰ J. T. Chalker and P. D. Coddington, J. Phys. C **21**, 2665 (1988).
- ⁵¹ S. Hikami, A. I. Larkin and Y. Nagaoka, Prog. Theor. Phys. **63**, 707 (1980).
- ⁵² K. Nomura, S. Ryu, M. Koshino, C. Mudry, and A. Furusaki, Phys. Rev. Lett. **100**, 246806 (2008).
- ⁵³ R. J. Johnston and H. Kunz, J. Phys. C: Solid State Phys. **16**, 3895 (1983).
- ⁵⁴ A. MacKinnon and B. Kramer, Z. Phys. B **53**, 1 (1983).
- ⁵⁵ See Supplemental Materials.
- ⁵⁶ Y. Asada, K. Slevin, and T. Ohtsuki, Phys. Rev. Lett. **89**, 256601 (2002).
- ⁵⁷ J. L. Cardy, *Conformal Invariance in Phase Transition and Critical Phenomena*, vol. 11, edited by C. Domb and J. L. Lebowitz (Academic, New York, 1986).

- ⁵⁸ H. Obuse, S. Bera, A. W. W. Ludwig, I. A. Gruzberg, and F. Evers, arXiv:1304.6517.
- ⁵⁹ K.-I. Imura, M. Okamoto, Y. Yoshimura, Y. Takane, and T. Ohtsuki, Phys. Rev. B **86**, 245436 (2012).
- ⁶⁰ Y. Yoshimura, A. Matsumoto, Y. Takane, and K. -I. Imura, Phys. Rev. B **88**, 045408 (2013).
- ⁶¹ P. W. Brouwer and K. Frahm, Phys. Rev. B **53**, 1490 (1996).
- ⁶² B. Kramer, T. Ohtsuki, and S. Kettemann, Phys. Rep. **417**, 211 (2005).
- ⁶³ A. P. Schnyder, S. Ryu, A. Furusaki, and A. W. W. Ludwig, Phys. Rev. B **78**, 195125 (2008).
- ⁶⁴ A. Kitaev, AIP Conf. Proc. **1134**, 22 (2009).
- ⁶⁵ S. Ryu, A. P. Schnyder, A. Furusaki, and A. W. W. Ludwig, New J. Phys. **12**, 065010 (2010).
- ⁶⁶ H. Yao and S. Ryu, Phys. Rev. B **88**, 064507 (2013).
- ⁶⁷ C.-K. Chiu, H. Yao, and S. Ryu, Phys. Rev. B **88**, 075142 (2013).
- ⁶⁸ I. C. Fulga, B. van Heck, J. M. Edge, and A. R. Akhmerov, arXiv:1212.6191.
- ⁶⁹ C. Wu, B. A. Bernevig, and S.-C. Zhang, Phys. Rev. Lett. **96**, 106401 (2006).
- ⁷⁰ C. Xu and J. E. Moore, Phys. Rev. B **73**, 045322 (2006).
- ⁷¹ M. Levin and A. Stern, Phys. Rev. Lett. **103**, 196803 (2009).
- ⁷² L. Fidkowski and A. Kitaev, Phys. Rev. B **81**, 134509 (2010).
- ⁷³ L. Fidkowski and A. Kitaev, Phys. Rev. B **83**, 075103 (2011).
- ⁷⁴ A. M. Turner, F. Pollmann, and E. Berg, Phys. Rev. B **83**, 075102 (2011).
- ⁷⁵ Z. Wang, X.-L. Qi, and S.-C. Zhang, Phys. Rev. B **84**, 014527 (2011).
- ⁷⁶ T. Neupert, L. Santos, S. Ryu, C. Chamon, and C. Mudry, Phys. Rev. B **84**, 165107 (2011).
- ⁷⁷ S. Ryu, J. E. Moore, and A. W. W. Ludwig, Phys. Rev. B **85**, 045104 (2012).
- ⁷⁸ S. Ryu and S.-C. Zhang, Phys. Rev. B **85**, 245132 (2012).
- ⁷⁹ X. Chen, Z.-C. Gu, Z.-X. Liu, and X.-G. Wen, Phys. Rev. B **87**, 155114 (2013).
- ⁸⁰ Z.-C. Gu and X.-G. Wen, arXiv:1201.2648.
- ⁸¹ X.-L. Qi, New J. Phys. **15**, 065002 (2013).
- ⁸² C. M. Ho and J. T. Chalker, Phys. Rev. B **54**, 8708 (1996).
- ⁸³ A. W. W. Ludwig, M. P. A. Fisher, R. Shankar, and G. Grinstein, Phys. Rev. B **50**, 7526 (1994).

Supplemental Materials for “Spin-directed network model for the surface states of weak three-dimensional \mathbb{Z}_2 topological insulators”

In this supplemental material, we present the details of our finite-size scaling analysis.

We apply a finite-size scaling analysis to the normalized localization lengths defined in Secs. III B and IV B with the goal of studying the critical properties at the metal-insulator transition of the two-dimensional spin-directed \mathbb{Z}_2 network model, if any. To this end, the normalized localization lengths along the vertical Λ_\perp and horizontal Λ_\parallel directions of the two-dimensional network are calculated numerically by the transfer matrix method^{S1} as a function of δ^2 with fixed values of the intrinsic parameters t^2 and θ and the geometric parameter M , whereby the width M ranges from a minimal value M_{\min} to a maximal value M_{\max} . If $\mathbf{x} = \perp, \parallel$, a data set (for $\Lambda_{\mathbf{x}}$) is the set of numbers

$$\left\{ \Lambda_{\mathbf{x}}(\delta_i^2, M_j) \mid \delta_{\min}^2 \leq \delta_i^2 \leq \delta_{\max}^2, M_{\min} \leq M_j \leq M_{\max} \right\}, \quad (\text{S1})$$

with δ_i^2 belonging to one of the cuts (3.6), (3.9), and (3.10) in parameter space. The normalized localization lengths Λ_\perp and Λ_\parallel for the two-dimensional spin-directed \mathbb{Z}_2 network model are presented in Figs. 14, 15, 17, S1, and S2.

We extract the critical exponent ν for the power-law divergence of the localization length defined by

$$\xi \propto |\delta^2 - \delta_c^2|^{-\nu}, \quad (\text{S2})$$

where δ_c^2 denotes the critical point for the dimerization strength δ^2 , if any. It is well known that the normalized localization length near the Anderson transition obeys a scaling law (not necessarily a power law, though).^{S1}

We treat the scaling behavior of the inverse

$$\Gamma_{\mathbf{x}} := \Lambda_{\mathbf{x}}^{-1}, \quad \mathbf{x} \equiv \perp, \parallel, \quad (\text{S3})$$

of the normalized localization length $\Lambda_{\mathbf{x}}$, which is proportional to the Lyapunov exponent $X_{\mathbf{x},1}$, a random variable that is selfaveraging in the thermodynamic limit.^{S2} The error bars on $\Gamma_{\mathbf{x}}$ are easier to obtain than the error bars on $\Lambda_{\mathbf{x}}$.

We assume that $\Gamma_{\mathbf{x}}$ is a scaling function^{S3},

$$\Gamma_{\mathbf{x}} = F_{\mathbf{x}} \left(\chi M^{1/\nu}, \zeta M^y \right), \quad (\text{S4})$$

where χ and ζ are the relevant and first leading irrelevant scaling variables, respectively. The irrelevant exponent y satisfies $y < 0$. In the limit $M \rightarrow \infty$, we furthermore assume that the scaling law (S4) obeys a Taylor expansion in powers of the scaling fields χ and ζ about $\chi M^{1/\nu} = \zeta M^y = 0$ that we truncate to the order N_{rel} and $N_{\text{irr}}(p)$, respectively,

$$\Gamma_{\mathbf{x}} \approx \sum_{p=0}^{N_{\text{rel}}} \sum_{q=0}^{N_{\text{irr}}(p)} F_{\mathbf{x}}^{p,q} \chi^p \zeta^q M^{p/\nu + qy}. \quad (\text{S5})$$

Here, we have allowed for the possibility that $N_{\text{irr}}(p)$ depends on p . If we assume that the expansion coefficients $F_{\mathbf{x}}^{p,0}$ are all non-vanishing, we may then do the factorization

$$\Gamma_{\mathbf{x}} \approx \sum_{p=0}^{N_{\text{rel}}} F_{\mathbf{x}}^{p,0} \left(\chi M^{1/\nu} \right)^p \left[1 + \sum_{q=1}^{N_{\text{irr}}(p)} f_{\mathbf{x}}^{p,q} (\zeta M^y)^q \right],$$

$$f_{\mathbf{x}}^{p,q} := \frac{F_{\mathbf{x}}^{p,q}}{F_{\mathbf{x}}^{p,0}}. \quad (\text{S6})$$

It is an empirical fact that the fitting procedure (S6) is more stable than the fitting procedure (S5). Finally, we assume that

$$\chi := \delta^2 - \delta_c^2 \quad (\text{S7})$$

and

$$\zeta = 1. \quad (\text{S8})$$

In other words, we choose as the fitting parameters the scaling exponents

$$\nu, \quad y, \quad (\text{S9a})$$

the location of the critical point

$$\delta_c^2, \quad (\text{S9b})$$

the $(N_{\text{rel}} + 1)$ expansion coefficients for the relevant perturbation

$$F_{\mathbf{x}}^{p,0}, \quad p = 0, \dots, N_{\text{rel}}, \quad (\text{S9c})$$

and the $\sum_{p=0}^{N_{\text{rel}}} N_{\text{irr}}(p)$ expansion coefficients for the leading irrelevant perturbation

$$f_{\mathbf{x}}^{p,q}, \quad q = 1, \dots, N_{\text{irr}}(p), \quad p = 0, \dots, N_{\text{rel}}. \quad (\text{S9d})$$

We call

$$\Lambda_{\mathbf{x}}^c := \frac{1}{F_{\mathbf{x}}^{0,0}}, \quad (\text{S10})$$

the universal scaling amplitude of the normalized localization lengths with $\mathbf{x} = \perp, \parallel$, respectively.

The quality of the fit of the data set to the scaling function is tested as follows. The simplest test for fitting numerical data is given by

$$\frac{\chi^2}{N} := \frac{1}{N} \sum_O \frac{(O - E)^2}{\sigma^2}, \quad (\text{S11})$$

where O runs over the N data, σ^2 is the variance of the data, and E is the value of the fitting function computed from Eq. (S6) corresponding to data O . Another measure for the quality of the fitting procedure is the goodness of fit Q defined by

$$Q := \Gamma_{\text{ni}}\left((N-p)/2, \chi^2/2\right), \quad (\text{S12a})$$

where

$$\Gamma_{\text{ni}}(a, x) := \frac{1}{\Gamma(a)} \int_x^\infty dt t^{a-1} e^{-t} \quad (\text{S12b})$$

denotes the normalized incomplete gamma function. The values of χ^2/N are distributed in the range $[0, \infty[$. A perfect fit gives $\chi^2/N = 0$. The values of Q are distributed in the range $[0, 1]$. A perfect fit gives $Q = 1$. In practice, a fit is acceptable if χ^2/N is smaller than 1.

A consistency check on the fitting procedure is obtained by verifying that the statistical error bar (one sigma) on a fitting parameter does not exceed the value of the fitting parameter by an order of magnitude one or more. Error bars of fitting parameters are themselves estimated from error-propagation theory given the error bars of Λ_x .

The fitting with the nonlinear function (S6) strongly depends on the initial values of the fitting parameters. For this reason, we perform iteratively the fitting for the

data set with different initial values of the fitting parameters. We then select the best fitting parameters as the ones with the smallest value of χ^2/N , that we denote χ_{min}^2/N . The best fitting parameters and their χ_{min}^2/N define the most reliable fit for a given data set. The typical number of iterations done for a given data set is about 1000.

The best fitting parameters should not depend on the given data set. For this reason, we repeat our scaling analysis for data sets differing through the choice of their minimum and maximum values M_{min} and M_{max} for the width of the quasi-one-dimensional spin-directed \mathbb{Z}_2 network model.

The list of fitting parameters obtained from this procedure is shown in Tables S-I–S-VI. Figures 14, S1, and S2 demonstrate that, for any one of $x = \perp, \parallel$,

$$\Lambda'_x := \Lambda_x - \sum_{p=0}^{N_{\text{rel}}} \sum_{q=1}^{N_{\text{irr}}(p)} F_x^{p,0} f_x^{p,q} \left(\chi M^{1/\nu} \right)^p M^{qy} \quad (\text{S13})$$

obeys a single-parameter scaling law. We have chosen for Figs. 14, S1, and S2 the fitting parameters (S9) with the smallest χ_{min}^2/N (S11) for the data set (S1) with the smallest and largest width M of the network model.

Inspection of Tables S-I–S-VI shows that the fitting parameters obtained from data sets with different minimum M_{min} and maximum M_{max} widths are not always consistent with each other.^{S4} To overcome this difficulty, we estimate the error bars on the fitting parameters presented in Table. I by making use of the practical-error-bar procedure from Ref. S5 applied to Tables S-I–S-VI.

^{S1} A. MacKinnon and B. Kramer, Z. Phys. B **53**, 1 (1983).

^{S2} R. J. Johnston and H. Kunz, J. Phys. C: Solid State Phys. **16**, 3895 (1983).

^{S3} See K. Slevin and T. Ohtsuki, Phys. Rev. Lett. **82**, 382 (1999) and references therein.

^{S4} When we calculated the fitting parameters by varying the minimum and maximum widths M_{min} and M_{max} , respectively, we noticed that the values of the fitting parameters were not always consistent with the statistical error bars even though χ_{min}^2/N and Q were acceptable. On the one hand, Table S-I gives values of ν from all data set that vary within the statistical error bars. On the other hand,

Table S-II gives values of ν extracted from the data set with $M_{\text{min}} = 16$ and $M_{\text{max}} = 256$ that are not within the error bars from the values of ν extracted from the data set with $M_{\text{min}} = 32$ and $M_{\text{max}} = 256$, while both set of values are statistically reliable as measured by χ_{min}^2/N . We believe that the reason for this inconsistency originates from the orders of truncations N_{rel} and $N_{\text{irr}}(p)$ in Eq. (S6), constrained as they are by the accuracy of our data, being too small.

^{S5} H. Obuse, S. Bera, A. W. W. Ludwig, I. A. Gruzberg, and F. Evers, arXiv:1304.6517.

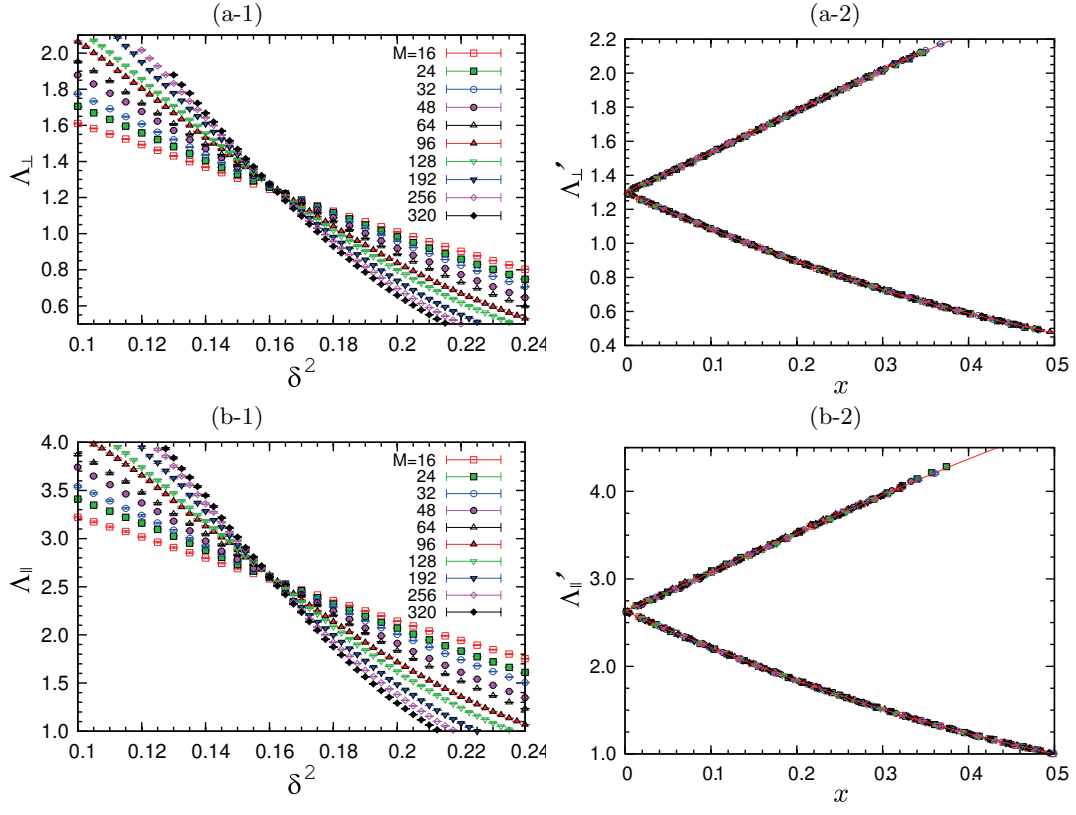


FIG. S1. (Color online:) The two-dimensional spin-directed \mathbb{Z}_2 network model is solved numerically along the one-dimensional cut (3.9) in the three-dimensional parameter space (2.7). Panel (a-1) shows the δ^2 dependence of the normalized localization length Λ_{\perp} corresponding to the geometry of Fig. 13(a) for several values of M . Panel (b-1) shows the δ^2 dependence of the normalized localization lengths Λ_{\parallel} corresponding to the geometry of Fig. 13(b) for several values of M . A finite-size scaling analysis of panels (a-1) and (b-1) is performed in panels (a-2) and (b-2), respectively. The horizontal axis is $x = M^{1/\nu}|\delta^2 - \delta_c^2|$ with ν and δ_c^2 given in Table S-III and Table S-IV. The vertical axis Λ'_x with $x = \perp, \parallel$ is defined by subtracting from the normalized localization length Λ_x its finite-size correction from the leading irrelevant exponent y given in Table S-III and Table S-IV. The red solid curve demonstrates the quality of the data collapse onto a one-parameter scaling function.

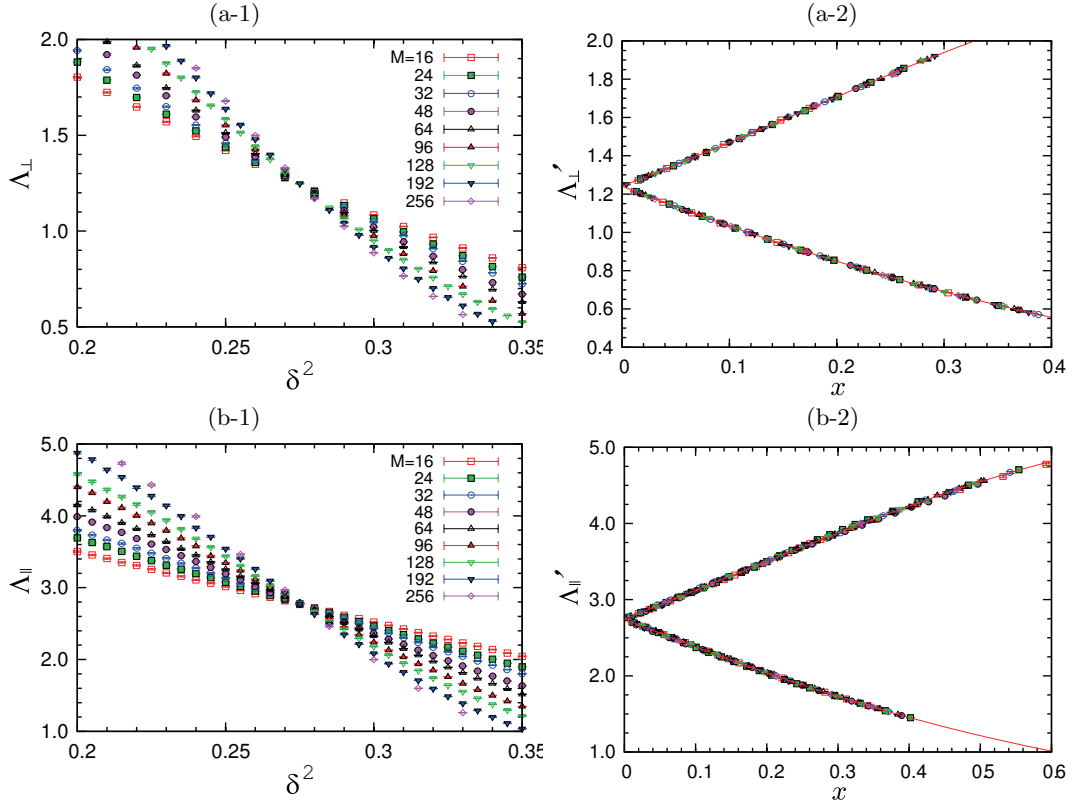


FIG. S2. (Color online:) The two-dimensional spin-directed \mathbb{Z}_2 network model is solved numerically along the one-dimensional cut (3.10) in the three-dimensional parameter space (2.7). Panel (a-1) shows the δ^2 dependence of the normalized localization length Λ_{\perp} corresponding to the geometry of Fig. 13(a) for several values of M . Panel (b-1) shows the δ^2 dependence of the normalized localization lengths Λ_{\parallel} corresponding to the geometry of Fig. 13(b) for several values of M . A finite-size scaling analysis of panels (a-1) and (b-1) is performed in panels (a-2) and (b-2), respectively. The horizontal axis is $x = M^{1/\nu}|\delta^2 - \delta_c^2|$ with ν and δ_c^2 given in Table S-V and Table S-VI. The vertical axis Λ'_x with $x = \perp, \parallel$ is defined by subtracting from the normalized localization length Λ_x its finite-size correction from the leading irrelevant exponent y given in Table S-V and Table S-VI. The red solid curve demonstrates the quality of the data collapse onto a one-parameter scaling function.

TABLE S-I. Finite-size scaling analysis of Λ_\perp for the two-dimensional spin-directed \mathbb{Z}_2 network model along the cut (3.6) $[(0.5, \pi/4, \delta^2)]$. Only the values of Λ_\perp satisfying $0.35 < \Lambda_\perp < 1.7$ enter the data set. Different data sets are chosen by varying the minimum M_{\min} and maximum M_{\max} taken by the width M of the two-dimensional spin-directed \mathbb{Z}_2 network model. The quality of fit is measured by χ^2_{\min}/N and Q . The values ν , y , δ_c^2 , Λ_\perp^c , $F_\perp^{p,0}$, and $f_\perp^{p,q}$ for the fitting parameters and their χ^2_{\min}/N are shown. The numbers with \pm are the statistical error bars (one sigma).

M_{\min}	M_{\max}	N	χ^2_{\min}/N	Q	ν	$ y $	δ_c^2	$\Lambda_\perp^c \equiv (1/F_\perp^{0,0})$	$f_\perp^{0,1}$	$f_\perp^{0,2}$	$F_\perp^{1,0}$	$f_\perp^{1,1}$	$f_\perp^{1,2}$	$F_\perp^{2,0}$	$f_\perp^{2,1}$	$f_\perp^{2,2}$	$F_\perp^{3,0}$	$f_\perp^{3,1}$	$F_\perp^{4,0}$	$f_\perp^{4,1}$
16	320	461	1.009	0.246	2.922	0.712	0.2336	0.94135	0.2081	-1.132	2.060	1.567	-6.563	3.079	1.644	-2.246	2.803	5.169	0.993	31.085
					± 0.037	± 0.054	± 0.0002	± 0.00256	± 0.0323	± 0.302	± 0.065	± 0.108	± 1.397	± 0.175	± 0.210	± 0.918	± 0.272	± 0.279	± 0.257	± 4.513
24	320	402	0.920	0.714	2.926	0.788	0.2340	0.93539	0.1443	-0.937	2.090	1.883	-11.030	3.131	2.053	-5.646	2.903	6.115	1.102	36.256
					± 0.053	± 0.107	± 0.0002	± 0.00299	± 0.0766	± 0.803	± 0.090	± 0.283	± 6.088	± 0.251	± 0.406	± 4.032	± 0.392	± 0.876	± 0.364	± 5.269
32	320	361	0.946	0.543	2.850	0.728	0.2345	0.92583	-0.0657	0.683	1.989	2.028	-9.519	2.802	2.768	-6.529	2.434	6.600	0.845	33.365
					± 0.102	± 0.159	± 0.0004	± 0.00636	± 0.0955	± 0.670	± 0.174	± 0.425	± 8.209	± 0.481	± 0.630	± 6.497	± 0.698	± 1.015	± 0.544	± 6.811
16	256	421	1.043	0.118	2.880	0.675	0.2337	0.94084	0.1907	-0.948	1.994	1.647	-5.943	2.892	1.805	-2.000	2.510	5.481	0.789	34.324
					± 0.052	± 0.057	± 0.0002	± 0.00344	± 0.0353	± 0.260	± 0.092	± 0.144	± 1.183	± 0.239	± 0.271	± 0.848	± 0.359	± 0.395	± 0.320	± 8.998
24	256	362	0.947	0.539	2.845	0.701	0.2343	0.93049	0.0569	-0.314	1.970	1.903	-7.757	2.777	2.356	-4.043	2.361	6.403	0.725	39.007
					± 0.089	± 0.108	± 0.0003	± 0.00487	± 0.0728	± 0.441	± 0.153	± 0.242	± 3.745	± 0.407	± 0.490	± 2.723	± 0.591	± 0.621	± 0.477	± 12.878

TABLE S-II. Finite-size scaling analysis of Λ_{\perp} for the two-dimensional spin-directed \mathbb{Z}_2 network model along the cut (3.6) $[(0.5, \pi/4, \delta^2)]$. Only the values of Λ_{\perp} satisfying $1.4 < \Lambda_{\perp} < 6.0$ enter the data set. Different data sets are chosen by varying the minimum M_{\min} and maximum M_{\max} taken by the width M of the two-dimensional spin-directed \mathbb{Z}_2 network model. The quality of fit is measured by χ^2_{\min}/N and Q . The values ν , y , δ_c^2 , Λ_{\parallel}^c , $F_{\parallel}^{p,0}$, and $f_{\parallel}^{p,q}$ for the fitting parameters and their χ^2_{\min}/N are shown. The numbers with \pm are the statistical error bars (one sigma).

M_{\min}	M_{\max}	N	χ^2_{\min}/N	Q	ν	$ y $	δ_c^2	Λ_{\parallel}^c	$(1/F_{\parallel}^{0,0})$	$f_{\parallel}^{0,1}$	$F_{\parallel}^{1,0}$	$f_{\parallel}^{1,1}$	$F_{\parallel}^{2,0}$	$f_{\parallel}^{2,1}$	$F_{\parallel}^{3,0}$	$f_{\parallel}^{3,1}$	$F_{\parallel}^{4,0}$	$f_{\parallel}^{4,1}$
16	256	403	0.941	0.641	2.793	0.404	0.2336		3.70707	0.041	0.562	-0.789	0.954	-0.967	1.004	-0.974	0.626	-0.735
					± 0.052	± 0.053	± 0.0003		± 0.01882	± 0.010	± 0.031	± 0.034	± 0.096	± 0.041	± 0.147	± 0.094	± 0.135	± 0.442
24	256	352	0.970	0.450	2.758	0.387	0.2340		3.67677	0.013	0.556	-0.745	0.903	-0.807	0.920	-0.774	0.615	-0.972
					± 0.067	± 0.083	± 0.0003		± 0.02158	± 0.014	± 0.045	± 0.055	± 0.129	± 0.065	± 0.186	± 0.149	± 0.168	± 0.397
32	256	307	0.875	0.852	2.653	0.473	0.2352		3.58849	-0.088	0.511	-0.801	0.747	-0.580	0.709	-0.547	0.444	-1.156
					± 0.059	± 0.125	± 0.0003		± 0.02051	± 0.030	± 0.039	± 0.146	± 0.093	± 0.130	± 0.127	± 0.257	± 0.117	± 0.740
16	192	361	0.943	0.606	2.772	0.449	0.2335		3.71150	0.049	0.543	-0.828	0.904	-1.008	0.924	-0.948	0.576	-0.659
					± 0.063	± 0.068	± 0.0003		± 0.02286	± 0.012	± 0.034	± 0.052	± 0.104	± 0.055	± 0.153	± 0.128	± 0.140	± 0.586
24	192	310	0.980	0.381	2.702	0.476	0.2340		3.67609	0.016	0.517	-0.818	0.799	-0.803	0.767	-0.595	0.514	-0.980
					± 0.073	± 0.114	± 0.0004		± 0.02398	± 0.019	± 0.041	± 0.115	± 0.113	± 0.094	± 0.152	± 0.249	± 0.143	± 0.595
32	192	265	0.866	0.842	2.578	0.632	0.2356		3.57956	-0.157	0.472	-1.038	0.646	-0.394	0.573	-0.045	0.362	-1.722
					± 0.051	± 0.175	± 0.0003		± 0.02268	± 0.073	± 0.029	± 0.361	± 0.063	± 0.250	± 0.080	± 0.566	± 0.082	± 1.415

TABLE S-III. Finite-size scaling analysis of Λ_{\perp} for the two-dimensional spin-directed \mathbb{Z}_2 network model along the cut (3.9) $[(0.5, 5\pi/16, \delta^2)]$. Only the values of Λ_{\perp} satisfying $0.45 < \Lambda_{\perp} < 2.15$ enter the data set. Different data sets are chosen by varying the minimum M_{\min} and maximum M_{\max} taken by the width M of the two-dimensional spin-directed \mathbb{Z}_2 network model. The quality of fit is measured by χ^2_{\min}/N and Q . The values ν , y , δ_c^2 , Λ_{\perp}^c , $F_{\perp}^{p,0}$, and $f_{\perp}^{p,q}$ for the fitting parameters and their χ^2_{\min}/N are shown. The numbers with \pm are the statistical error bars (one sigma).

M_{\min}	M_{\max}	N	χ^2_{\min}/N	Q	ν	$ y $	δ_c^2	$\Lambda_{\perp}^c \equiv (1/F_{\perp}^{0,0})$	$f_{\perp}^{0,1}$	$f_{\perp}^{0,2}$	$F_{\perp}^{1,0}$	$f_{\perp}^{1,1}$	$f_{\perp}^{1,2}$	$F_{\perp}^{2,0}$	$f_{\perp}^{2,1}$	$F_{\perp}^{3,0}$	$f_{\perp}^{3,1}$	$F_{\perp}^{4,0}$
12	320	528	1.067	0.064	2.743	0.580	0.1588	1.30050	0.0919	0.446	1.332	1.204	-4.489	1.741	1.515	1.439	0.887	0.999
					± 0.021	± 0.032	± 0.0002	± 0.00381	± 0.0354	± 0.051	± 0.030	± 0.083	± 0.344	± 0.072	± 0.072	± 0.086	± 0.190	± 0.046
16	320	477	1.019	0.223	2.731	0.625	0.1595	1.28399	-0.0079	0.911	1.350	1.162	-5.039	1.743	1.722	1.428	1.015	0.960
					± 0.025	± 0.045	± 0.0002	± 0.00500	± 0.0497	± 0.109	± 0.033	± 0.080	± 0.735	± 0.085	± 0.079	± 0.098	± 0.215	± 0.054
32	320	373	0.751	0.999	2.688	0.729	0.1611	1.24759	-0.4620	4.587	1.362	1.361	-8.908	1.722	2.422	1.364	1.643	0.717
					± 0.045	± 0.111	± 0.0005	± 0.01359	± 0.0893	± 2.293	± 0.050	± 0.208	± 5.160	± 0.144	± 0.323	± 0.163	± 0.389	± 0.086
12	256	491	1.040	0.139	2.765	0.613	0.1584	1.30826	0.1600	0.343	1.357	1.143	-4.870	1.806	1.486	1.498	0.885	1.066
					± 0.025	± 0.041	± 0.0002	± 0.00417	± 0.0457	± 0.069	± 0.036	± 0.105	± 0.483	± 0.087	± 0.081	± 0.101	± 0.211	± 0.055
16	256	440	0.974	0.453	2.867	1.413	0.1592	1.28935	2.1767	-35.927	1.529	0.119	-86.394	2.219	6.329	1.906	0.946	1.322
					± 0.006	± 0.080	± 0.0001	± 0.00206	± 0.5515	± 21.322	± 0.006	± 0.384	± 27.812	± 0.018	± 1.310	± 0.023	± 0.906	± 0.032
12	192	450	0.863	0.952	2.905	1.118	0.1581	1.30627	1.1074	-5.450	1.540	0.063	-18.218	2.271	2.295	1.987	0.220	1.435
					± 0.008	± 0.069	± 0.0002	± 0.00391	± 0.1953	± 2.435	± 0.009	± 0.227	± 3.708	± 0.025	± 0.338	± 0.031	± 0.361	± 0.034
16	192	399	0.822	0.984	2.883	1.307	0.1587	1.29607	1.7245	-19.092	1.535	-0.022	-48.366	2.237	4.543	1.924	1.295	1.377
					± 0.009	± 0.095	± 0.0002	± 0.00330	± 0.4923	± 13.253	± 0.009	± 0.422	± 16.502	± 0.026	± 1.051	± 0.032	± 0.768	± 0.036

TABLE S-IV. Finite-size scaling analysis of Λ_{\perp} for the two-dimensional spin-directed \mathbb{Z}_2 network model along the cut (3.9) $[(0.5, 5\pi/16, \delta^2)]$. Only the values of Λ_{\parallel} satisfying $1.0 < \Lambda_{\parallel} < 4.0$ enter the data set. Different data sets are chosen by varying the minimum M_{\min} and maximum M_{\max} taken by the width M of the two-dimensional spin-directed \mathbb{Z}_2 network model. The quality of fit is measured by χ^2_{\min}/N and Q . The values ν , y , δ_c^2 , Λ_c^c , $F_{\parallel}^{p,0}$, and $f_{\parallel}^{p,q}$ for the fitting parameters and their χ^2_{\min}/N are shown. The numbers with \pm are the statistical error bars (one sigma).

M_{\min}	M_{\max}	N	χ^2_{\min}/N	Q	ν	$ y $	δ_c^2	$\Lambda_c^c \equiv (1/F_{\parallel}^{0,0})$	$f_{\parallel}^{0,1}$	$F_{\parallel}^{1,0}$	$f_{\parallel}^{1,1}$	$F_{\parallel}^{2,0}$	$f_{\parallel}^{2,1}$	$F_{\parallel}^{3,0}$	$f_{\parallel}^{3,1}$	$F_{\parallel}^{4,0}$	$f_{\parallel}^{4,1}$
16	320	450	0.926	0.752	2.585	1.355	0.1595	2.63191	0.812	0.622	-3.609	0.835	-2.811	0.667	-17.095	0.266	28.211
					± 0.008	± 0.057	± 0.0001	± 0.00344	± 0.105	± 0.003	± 0.498	± 0.010	± 0.504	± 0.017	± 2.850	± 0.028	± 13.114
24	320	392	0.925	0.717	2.627	1.102	0.1591	2.64418	0.476	0.640	-1.779	0.888	-2.039	0.751	-10.540	0.312	4.511
					± 0.018	± 0.115	± 0.0002	± 0.00677	± 0.129	± 0.008	± 0.516	± 0.024	± 0.514	± 0.041	± 3.242	± 0.039	± 7.585
32	320	341	0.987	0.358	2.637	1.089	0.1590	2.64916	0.544	0.643	-1.715	0.902	-2.504	0.768	-10.699	0.326	4.774
					± 0.028	± 0.202	± 0.0002	± 0.01055	± 0.282	± 0.012	± 0.916	± 0.039	± 1.139	± 0.064	± 6.135	± 0.048	± 11.316
48	320	295	1.096	0.045	2.625	1.387	0.1591	2.64608	1.670	0.638	-5.847	0.882	-5.912	0.711	-12.797	0.359	-50.833
					± 0.035	± 0.478	± 0.0003	± 0.01358	± 2.519	± 0.016	± 9.286	± 0.048	± 7.724	± 0.065	± 19.002	± 0.065	± 102.505
16	256	415	0.904	0.827	2.588	1.333	0.1593	2.63549	0.801	0.623	-3.449	0.837	-2.656	0.666	-15.829	0.267	25.730
					± 0.010	± 0.062	± 0.0001	± 0.00428	± 0.109	± 0.004	± 0.509	± 0.012	± 0.489	± 0.020	± 2.812	± 0.030	± 12.860
24	256	357	0.911	0.760	2.663	0.947	0.1587	2.66138	0.376	0.654	-1.280	0.934	-1.647	0.822	-6.982	0.342	2.410
					± 0.029	± 0.127	± 0.0003	± 0.01149	± 0.101	± 0.013	± 0.365	± 0.041	± 0.375	± 0.071	± 2.208	± 0.052	± 5.035
32	256	306	0.970	0.427	2.721	0.763	0.1581	2.68761	0.307	0.679	-0.869	1.021	-1.455	0.952	-4.433	0.421	0.027
					± 0.068	± 0.217	± 0.0005	± 0.02842	± 0.131	± 0.033	± 0.373	± 0.112	± 0.502	± 0.190	± 2.298	± 0.106	± 3.875
16	192	377	0.886	0.867	2.561	1.464	0.1596	2.62681	1.038	0.613	-4.543	0.812	-3.431	0.628	-22.355	0.233	51.727
					± 0.011	± 0.074	± 0.0002	± 0.00483	± 0.169	± 0.004	± 0.803	± 0.013	± 0.748	± 0.020	± 4.719	± 0.029	± 23.579
24	192	319	0.920	0.686	2.638	1.062	0.1589	2.65335	0.491	0.642	-1.591	0.907	-2.226	0.777	-9.744	0.280	10.521
					± 0.033	± 0.161	± 0.0004	± 0.01315	± 0.172	± 0.014	± 0.593	± 0.044	± 0.687	± 0.074	± 4.032	± 0.050	± 10.589
32	192	268	0.982	0.349	2.697	0.889	0.1582	2.68162	0.442	0.664	-1.065	0.991	-2.178	0.903	-6.721	0.313	8.302
					± 0.081	± 0.301	± 0.0007	± 0.03407	± 0.287	± 0.035	± 0.681	± 0.123	± 1.278	± 0.206	± 5.229	± 0.088	± 12.495

TABLE S-V. Finite size scaling analysis of Λ_{\parallel} for the two-dimensional spin-directed \mathbb{Z}_2 network model along the cut (3.10) $[(0.6, \pi/4, \delta^2)]$. Only the values of Λ_{\perp} satisfying $0.5 < \Lambda_{\perp} < 2.0$ enter the data set. Different data sets are chosen by varying the minimum M_{\min} and maximum M_{\max} taken by the width M of the two-dimensional spin-directed \mathbb{Z}_2 network model. The quality of fit is measured by χ^2_{\min}/N and Q . The values ν , y , δ_c^2 , Λ_{\perp}^c , $F_{\perp}^{p,0}$, and $f_{\perp}^{p,q}$ for the fitting parameters and their χ^2_{\min}/N are shown. The numbers with \pm are the statistical error bars (one sigma).

M_{\min}	M_{\max}	N	χ^2_{\min}/N	Q	ν	$ y $	δ_c^2	$\Lambda_{\perp}^c \equiv (1/F_{\perp}^{0,0})$	$f_{\perp}^{0,1}$	$f_{\perp}^{0,2}$	$F_{\perp}^{1,0}$	$f_{\perp}^{1,1}$	$f_{\perp}^{1,2}$	$F_{\perp}^{2,0}$	$f_{\perp}^{2,1}$	$F_{\perp}^{3,0}$	$f_{\perp}^{3,1}$	$F_{\perp}^{4,0}$
16	256	172	0.570	1.000	2.837	0.713	0.2756	1.24122	0.1135	-0.861	1.420	1.861	-5.834	1.852	1.835	1.507	3.884	1.226
					± 0.069	± 0.138	± 0.0004	± 0.00760	± 0.0579	± 0.523	± 0.097	± 0.280	± 3.660	± 0.223	± 0.205	± 0.302	± 0.639	± 0.205
24	256	150	0.536	1.000	2.810	0.764	0.2763	1.22920	-0.0080	-0.374	1.416	2.138	-8.279	1.814	2.293	1.436	5.463	1.098
					± 0.107	± 0.253	± 0.0005	± 0.00993	± 0.1141	± 0.916	± 0.139	± 0.949	± 12.369	± 0.337	± 0.555	± 0.453	± 1.618	± 0.280
16	192	162	0.513	1.000	2.865	0.819	0.2764	1.22782	0.0032	-0.729	1.487	1.993	-8.833	1.973	2.006	1.674	4.180	1.323
					± 0.068	± 0.163	± 0.0004	± 0.00701	± 0.0752	± 0.638	± 0.084	± 0.453	± 6.916	± 0.206	± 0.308	± 0.285	± 0.899	± 0.215
24	192	140	0.426	1.000	2.830	0.938	0.2776	1.20775	-0.4189	3.267	1.493	2.702	-19.406	1.938	3.108	1.599	7.578	1.167
					± 0.094	± 0.270	± 0.0008	± 0.01461	± 0.2471	± 4.782	± 0.098	± 1.621	± 32.971	± 0.264	± 1.190	± 0.365	± 3.573	± 0.260

